

# NOMU: Neural Optimization-based Model Uncertainty

Jakob Heiss\*

jakob.heiss@math.ethz.ch  
ETH ZURICH

Jakob Weissteiner\*

weissteiner@ifi.uzh.ch  
UNIVERSITY OF ZURICH

Hanna Wutte\*

hanna.wutte@math.ethz.ch  
ETH ZURICH

Sven Seuken

seuken@ifi.uzh.ch  
UNIVERSITY OF ZURICH

Josef Teichmann

josef.teichmann@math.ethz.ch  
ETH ZURICH

## Abstract

We introduce a new approach for capturing model uncertainty for neural networks (NNs) in regression, which we call *Neural Optimization-based Model Uncertainty (NOMU)*. The main idea of NOMU is to design a network architecture consisting of two connected sub-networks, one for the model prediction and one for the model uncertainty, and to train it using a carefully designed loss function. With this design, NOMU can provide model uncertainty for any given (previously trained) NN by plugging it into the framework as the sub-network used for model prediction. NOMU is designed to yield uncertainty bounds (UBs) that satisfy four important desiderata regarding model uncertainty, which established methods often do not satisfy. Furthermore, our UBs are themselves representable as a *single* NN, which leads to computational cost advantages in applications such as Bayesian optimization. We evaluate NOMU experimentally in multiple settings. For regression, we show that NOMU performs as well as or better than established benchmarks. For Bayesian optimization, we show that NOMU outperforms all other benchmarks.

## 1. Introduction

Neural networks (NNs) are becoming increasingly important in machine learning applications (LeCun et al., 2015). In many domains, it is essential to be able to quantify the *uncertainty* of the NN predictions (Neal, 2012; Ghahramani, 2015). In applications such as autonomous driving or automated passport control, overconfident predictions can even be dangerous (Amodei et al., 2016). Good estimates of a model prediction’s uncertainty are particularly important in Bayesian optimization (BO) and active learning, where exploration is steered by (functions of) these uncertainty estimates. BO has been successfully applied in practice

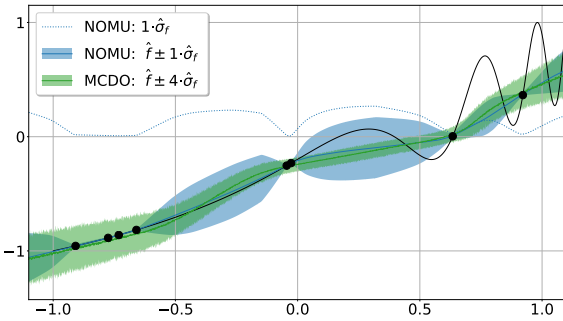


Figure 1. Example visualization of model uncertainty. The unknown true function is depicted as a black solid line with corresponding training points as black dots. NOMU’s mean prediction  $\hat{f}$  is shown as a solid blue line and its UBs are the blue shaded area. NOMU’s estimated model uncertainty  $\hat{\sigma}_f$  is separately shown as a blue dotted line. As a benchmark, MC dropout is shown in green.

to a wide range of problems, including robotics (Martinez-Cantin et al., 2009), sensor networks (Srinivas et al., 2012), and drug development (Gómez-Bombarelli et al., 2018). Better uncertainty estimates for BO directly translate to improvements in these applications.

In this paper, we study the problem of estimating *model uncertainty* for NNs to obtain *uncertainty bounds (UBs)* that mimic Bayesian credible bounds. Figure 1 shows an example visualization of UBs for NOMU and a benchmark.

### 1.1. Uncertainty Quantification for Neural Networks

Over the last decade, researchers have developed various methods to quantify uncertainty for NNs. One strand of research considers Bayesian Neural Networks (BNNs), where distributions are placed over the NN’s parameters (Graves, 2011; Blundell et al., 2015; Hernández-Lobato & Adams, 2015). But these methods are usually computationally prohibitive and require careful hyperparameter tuning. Therefore, BNNs are rarely used in practice (Wenzel et al., 2020).

In practice, *ensemble methods* (i.e., using a collection of NNs) are more established. Gal & Ghahramani (2016) proposed the *Monte Carlo (MC) dropout* algorithm to esti-

\*Equal contribution

mate model uncertainty via stochastic forward passes in the NN. Interestingly, they could show that training a NN with dropout regularization can also be interpreted as approximate Bayesian inference. [Lakshminarayanan et al. \(2017\)](#) experimentally evaluated ensembles of NNs and showed that they perform as good or better than BNNs. They proposed using *deep ensembles*, which use NNs with two outputs for mean and data noise, and they estimate model uncertainty via the empirical standard deviation of the ensemble.

Despite the popularity of MC dropout and deep ensembles, our empirical results suggest that none of them reliably capture all essential features of model uncertainty. MC dropout yields tubular bounds that do not narrow at observed data points (see MCDO in Figure 1). Deep ensembles can produce UBS that are sometimes unreasonably narrow in regions far from the data or unreasonably wide at observed data points. Moreover, in all methods discussed above, calculating UBS at a single input point requires multiple evaluations of different NNs. This leads to high computational and memory costs, which may be prohibitive in applications like BO, where the NNs must be evaluated frequently.

## 1.2. Overview of Our Contribution

We present a completely new approach for estimating model uncertainty for NNs, which we call *neural optimization based model uncertainty (NOMU)*. In contrast to a fully Bayesian approach (e.g. BNNs), where approximating the posterior for a realistic prior is in general very challenging, we approximate posterior credible bounds by directly enforcing four essential features of model uncertainty. Specifically, we make the following contributions:

1. We first introduce four desiderata that we argue uncertainty bounds should satisfy (Section 3.1).
2. We then introduce NOMU, which consists of a network architecture (Section 3.2) and a carefully-designed loss function (Section 3.3), such that the estimated UBS fulfill these four desiderata. NOMU is easy to implement, scales well to large NNs and can be represented as a single NN in contrast to ensemble methods. Because of its modular architecture, it can easily be used to obtain UBS for already trained NNs. Furthermore, we provide a theoretical motivation for our algorithm (Section 4).
3. We conduct an experimental study for regression based on synthetic and real data. Specifically, we measure the quality of NOMU UBS and benchmark them against the following state-of-the-art methods: MC dropout, deep ensembles and Gaussian processes. Overall, our experiments suggest that NOMU performs as good or better than these benchmarks (Section 5.1).
4. Finally, we evaluate the performance of NOMU in high-dimensional BO tasks, where we show that NOMU outperforms all considered benchmarks (Section 5.2).

## 1.3. Further Related Work

[Khosravi et al. \(2010\)](#) and [Pearce et al. \(2018\)](#) previously considered NNs with two outputs for lower and upper UBS, trained on a specifically designed loss functions. However, [Khosravi et al. \(2010\)](#) only accounted for data noise and did not consider model uncertainty. Similarly, [Pearce et al. \(2018\)](#) did not account for model uncertainty in the design of their loss function and only incorporate it via ensembles (as in deep ensembles). [Kendall & Gal \(2017\)](#) used MC dropout for model uncertainty and combined it with the idea by [Nix & Weigend \(1994\)](#) of directly modeling mean and data noise as network outputs. [Wang et al. \(2019\)](#) and [Wen et al. \(2020\)](#) refined ensemble methods for NNs by further promoting their diversity on the function space and by reducing their computational cost, respectively. For classification, [Malinin & Gales \(2018\)](#) introduced prior networks, which explicitly model in-sample and out-of-sample uncertainty, where the latter is realized by minimizing the reverse KL-distance to a selected flat pointwise defined prior. In a recent working paper (and concurrent to our work), [Malinin et al. \(2020\)](#) report on progress extending their idea to regression.

## 2. Preliminaries

In this section, we briefly review the standard Bayesian uncertainty framework for regression.

Let  $X \subset \mathbb{R}^d, Y \subset \mathbb{R}$  and let  $f: X \rightarrow Y$  denote the unknown ground truth function. Let  $D^{\text{train}} := \{(x_i^{\text{train}}, y_i^{\text{train}}) \in X \times Y, i \in \{1, \dots, n^{\text{train}}\}\}$ , with  $n^{\text{train}} \in \mathbb{N}$  denote i.i.d samples from the data generating process  $y = f(x) + \varepsilon$ , where  $\varepsilon|x \sim \mathcal{N}(0, \sigma_n^2(x))$ . We use  $\sigma_n$  to refer to the *data noise (aleatoric uncertainty)*. We refer to each  $(x_i^{\text{train}}, y_i^{\text{train}})$  as a *training point* and to each  $x_i^{\text{train}}$  as an *input training point*.

Given a prior distribution of  $f$  and known data noise  $\sigma_n$ , the posterior distributions of  $f$  and  $y$  are well defined. The *model uncertainty (epistemic uncertainty)*  $\sigma_f$  is the posterior standard deviation of  $f$ , i.e.,

$$\sigma_f(x) := \sqrt{\mathbb{V}[f(x)|D^{\text{train}}]}, x \in X. \quad (1)$$

Assuming independence between  $f$  and  $\varepsilon$ , the variance of the predictive distribution of  $y$  can be decomposed as  $\mathbb{V}[y|D^{\text{train}}, x] = \sigma_f^2(x) + \sigma_n^2(x)$ .

Given some  $\alpha \in [0, 1]$ , *credible bounds (CBs)*  $\underline{CB}$  and  $\overline{CB}$  fulfill that  $\mathbb{P}[f(x) \in [\underline{CB}, \overline{CB}]|D^{\text{train}}, x] = \alpha$ .<sup>1</sup> We present our algorithm for estimating model uncertainty for the case of zero or negligible data noise, i.e.,  $\sigma_n \approx 0$ .<sup>2</sup>

<sup>1</sup>For  $\sigma_n \equiv 0$ , CBs are equal to *predictive bounds*  $\underline{PB}, \overline{PB}$  with  $\mathbb{P}[y \in [\underline{PB}, \overline{PB}]|D^{\text{train}}, x] = \alpha$ . Otherwise, PBs are wider.

<sup>2</sup>For  $\sigma_n \gg 0$ , see our extension in Appendix C.1

### 3. The NOMU Algorithm

In this section, we present NOMU. We design NOMU to yield a model prediction  $\hat{f} \in \mathbb{R}$  and a model uncertainty prediction  $\hat{\sigma}_f \in \mathbb{R}_{>0}$ , such that the resulting UBs fulfill four important desiderata, which we introduce next.

#### 3.1. Desiderata

D1 (Non-Negativity) *The upper/lower UBs between two training points lie above/below the model prediction  $\hat{f}$ .*

D2 (In-Sample) *In the noiseless case, there is no (model) uncertainty at each input training point  $x^{train}$  (i.e., at  $x^{train}$  the upper and lower UBs are equal to  $\hat{f}(x^{train})$ .)*

D3 (Out-of-Sample) *The larger the distance to the input training points, the wider the UBs (i.e., model uncertainty increases out-of-sample).*

A priori, it is often not obvious which metric to choose in D3 to measure distances between input training points. In many applications, it is therefore best to *learn* this metric from the training data.<sup>3</sup>

D4 (Metric Learning) *Changes in those features of  $x$  that have high predictive power on the training set have a large effect on the distance metric used in D3.*

See Appendix A.4. for visualizations of D4.

#### 3.2. The Network Architecture

For NOMU, we construct a network  $\mathcal{NN}_\theta$  with two outputs: *the model prediction  $\hat{f}$*  (e.g. mean prediction) and a *raw model uncertainty prediction  $\hat{r}_f$* . Formally:  $\mathcal{NN}_\theta: X \rightarrow Y \times \mathbb{R}_{\geq 0}$ , with

$$x \mapsto \mathcal{NN}_\theta(x) := (\hat{f}(x), \hat{r}_f(x)). \quad (2)$$

NOMU's architecture is highly modular, as it consists of two almost separate sub-networks: the  $\hat{f}$ -network and the  $\hat{r}_f$ -network (see Figure 2). For each sub-network, any network architecture can be used (e.g., feed-forward NNs, CNNs). Importantly, we can plug in any previously trained NN for  $\hat{f}$ , or we can train  $\hat{f}$  simultaneously with the  $\hat{r}_f$ -network. The  $\hat{r}_f$ -network learns the raw model uncertainty and is

<sup>3</sup>Consider the task of learning facial expressions from images. For this, eyes and mouth are important features, while background color is not. A CNN automatically learns which features are important for model prediction. The same features are also important for capturing model uncertainty. Consider an image with pixel values very similar to those of an image of the training data, but where mouth and eyes are very different. We should be substantially more uncertain about the model prediction for such an image than for one which is almost identical to a training image except that it has a different background color, even if this change of background color results in a huge Euclidean distance of the pixel vectors. D4 requires that a more useful distance metric is learned instead.

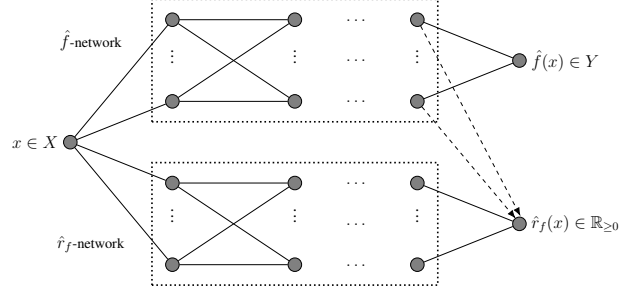


Figure 2. Schematic view of NOMU's network architecture

connected with the  $\hat{f}$ -network through the last hidden layer (dashed lines in Figure 2). This connection enables  $\hat{r}_f$  to re-use features that are important for the model prediction  $\hat{f}$ , implementing Desideratum D4 (Metric Learning).<sup>4</sup>

**Remark 3.1** *NOMU's network architecture can be modified to realize D4 (Metric Learning) in many different ways. For example, if low-level features were important for predicting the model uncertainty, one could additionally add connections from earlier hidden layers of the  $\hat{f}$ -network to layers of the  $\hat{r}_f$ -network. Furthermore, one can strengthen D4 (Metric Learning) by increasing the regularization of the  $\hat{r}_f$ -network (see Appendix A.4.).*

After training  $\mathcal{NN}_\theta$ , we apply the readout map  $\varphi(z) = \ell_{\max}(1 - \exp(-\frac{\max(0, z) + \ell_{\min}}{\ell_{\max}}))$  to the raw model uncertainty output  $\hat{r}_f$  to obtain the *model uncertainty prediction*

$$\hat{\sigma}_f(x) := \varphi(\hat{r}_f(x)), \forall x \in X. \quad (3)$$

The readout map  $\varphi$  monotonically interpolates between a minimal  $\ell_{\min}$  and a maximal  $\ell_{\max}$  model uncertainty. The parameter  $\ell_{\min}$  is used for numerical stability, and  $\ell_{\max}$  defines the maximal model uncertainty far away from input training points (similar to the prior variance in Gaussian processes). We can now define NOMU's uncertainty bounds:

**Definition 3.2** (NOMU UNCERTAINTY BOUNDS) *Let  $c \in \mathbb{R}_{\geq 0}$  denote a suitable calibration parameter.<sup>5</sup> For each  $x \in X$ , NOMU's UBs are defined as*

$$(\underline{UB}_c(x), \overline{UB}_c(x)) := (\hat{f}(x) \mp c \hat{\sigma}_f(x)). \quad (4)$$

It is straightforward to construct a *single* NN that directly outputs the upper (respectively the lower) UB, by extending the architecture shown in Figure 2: we transform and scale the output  $\hat{r}_f(x)$  and then add (respectively subtract) this to/from the other output  $\hat{f}(x)$ . It is also straightforward to compute NOMU's UBs for any given, previously trained

<sup>4</sup>To prevent that  $\hat{r}_f$  impacts the prediction  $\hat{f}$ , the dashed lines should only make forward passes during training.

<sup>5</sup>Like all other methods, NOMU outputs *relative* UBs that must be calibrated via a parameter  $c$  when used in practice.

NN, by attaching the  $\hat{r}_f$ -network to the trained NN, and only training the  $\hat{r}_f$ -network on the same training points used to train the original NN.

**Remark 3.3** *The choice of the readout map  $\varphi$  depends on the application. For example, for BO over discrete domains (e.g.  $X = \{0, 1\}^d$ ; see [Baptista & Poloczek \(2018\)](#)), we propose the readout map  $\varphi(z) = \ell_{\min} + \max(0, z - \ell_{\min}) - \max(0, z - \ell_{\max})$ . With this  $\varphi$  and ReLU activations, one can encode NOMU's UBS as a mixed integer program (MIP) ([Weissteiner & Seuken, 2020](#)). This enables optimizing the upper UBS as acquisition function without the need for further approximation via ensemble distillations, as is required for deep ensembles and MC dropout ([Malinin et al., 2019](#)).*

### 3.3. The Loss Function

We now introduce the loss function  $L^\pi$  we use for training NOMU's NN. In the following, let  $X$  be such that  $0 < \lambda_d(X) < \infty$  where  $\lambda_d$  denotes the  $d$ -dimensional Lebesgue measure.

We train  $\mathcal{NN}_\theta$  with loss  $L^\pi$  and L2-regularization parameter  $\lambda > 0$ , i.e., minimizing  $L^\pi(\mathcal{NN}_\theta) + \lambda \|\theta\|_2^2$  via a gradient descent based algorithm.

**Definition 3.4 (NOMU LOSS)** *Let  $\pi := (\pi_{\text{sqr}}, \pi_{\text{exp}}, c_{\text{exp}}) \in \mathbb{R}_{\geq 0}^3$  denote a tuple of hyperparameters. Given a training set  $D^{\text{train}}$ , the loss function  $L^\pi$  is defined as*

$$L^\pi(\mathcal{NN}_\theta) := \underbrace{\sum_{i=1}^{n^{\text{train}}} (\hat{f}(x_i^{\text{train}}) - y_i^{\text{train}})^2}_{(a)} + \pi_{\text{sqr}} \cdot \underbrace{\sum_{i=1}^{n^{\text{train}}} (\hat{r}_f(x_i^{\text{train}}))^2}_{(b)} + \pi_{\text{exp}} \cdot \underbrace{\frac{1}{\lambda_d(X)} \int_X e^{-c_{\text{exp}} \cdot \hat{r}_f(x)} dx}_{(c)}. \quad (5)$$

In the following, we explain how the three terms of  $L^\pi$  promote the desiderata we introduced in Section 3.1. Note that the behaviour of  $\hat{r}_f$  directly translates to that of  $\hat{\sigma}_f$ .

- Term (a) solves the regression task, i.e., it learns a smooth regularized function  $\hat{f}$  given  $D^{\text{train}}$ . If  $\hat{f}$  is given as a pre-trained NN, then this term can be omitted.
- Term (b) implements **D2 (In-Sample)** (i.e.,  $\hat{r}_f(x_i^{\text{train}}) \approx 0$  at input training points  $x_i^{\text{train}}$ ). The hyperparameter  $\pi_{\text{sqr}}$  controls the amount of uncertainty at the training points and can be adjusted to capture small data noise. The larger  $\pi_{\text{sqr}}$ , the narrower the UBS at training points.
- Term (c) has two purposes. First, it implements **D1 (Non-Negativity)** (i.e.,  $\hat{r}_f \geq 0$ ). Second, it pushes  $\hat{r}_f$  towards infinity across the whole input space  $X$ . However, due to the counteracting force of (b) as well as regularization,  $\hat{r}_f$  increases continuously as you move away from the training data. The interplay of (b), (c), and regularization thus promotes **D3 (Out-of-Sample)**. The hyperparameters

$\pi_{\text{exp}}$  and  $c_{\text{exp}}$  control the size and shape of the UBS. Concretely, the larger  $\pi_{\text{exp}}$ , the wider the UBS; the larger  $c_{\text{exp}}$ , the narrower the UBS at points  $x$  with large  $\hat{\sigma}_f(x)$  and the wider the UBS at points  $x$  with small  $\hat{\sigma}_f(x)$ .

In the implementation of  $L^\pi$ , we approximate (c) via MC-integration using additional, artificial input points  $D^{\text{art}} := \{x_i\}_{i=1}^l \stackrel{i.i.d.}{\sim} \text{Unif}(X)$  by  $\frac{1}{l} \cdot \sum_{x \in D^{\text{art}}} e^{-c_{\text{exp}} \cdot \hat{r}_f(x)}$ .

**Remark 3.5** *In (c), instead of the Lebesgue-measure, one can also use a different measure  $\nu$ , i.e.,  $\frac{1}{\nu(X)} \int_X e^{-c_{\text{exp}} \cdot \hat{r}_f(x)} d\nu(x)$ . This can be relevant in high dimensions, where meaningful data points often lie close to a lower-dimensional manifold ([Cayton, 2005](#));  $\nu$  can then be chosen to concentrate on that region. In practice, this can be implemented by sampling from a large unlabeled data set  $D^{\text{art}}$  representing this region. Alternatively, if no such data set is available, one can try to learn the measure  $\nu$  using GANs ([Goodfellow et al., 2014](#)).*

## 4. Theoretical Analysis

In this section, we provide a theoretical motivation for the design of NOMU. To this end, we first define worst case UBS that also have a probabilistic Bayesian interpretation. We then prove a theorem connecting these worst case bounds and NOMU's UBS via NOMU's loss function. In what follows, we assume zero data noise  $\sigma_n = 0$ .

Consider a hypothesis class  $\mathcal{H}$  given as a subset of a Banach space of functions  $f : X \rightarrow Y$ . Furthermore, let  $\mathcal{H}_{D^{\text{train}}} := \{f \in \mathcal{H} : f(x_i^{\text{train}}) = y_i^{\text{train}}, i = 1, \dots, n^{\text{train}}\}$  denote the set of all functions from the hypothesis class that fit through the training points and let  $\hat{f} \in \mathcal{H}_{D^{\text{train}}}$  be a prediction function (e.g., a NN trained on  $D^{\text{train}}$ ). Worst-case bounds within the class  $\mathcal{H}_{D^{\text{train}}}$  can be defined pointwise for each  $x \in X$  as:

$$\underline{UB}_{\text{pw}}(x) := \inf_{f \in \mathcal{H}_{D^{\text{train}}}} f(x), \quad (6)$$

$$\overline{UB}_{\text{pw}}(x) := \sup_{f \in \mathcal{H}_{D^{\text{train}}}} f(x). \quad (7)$$

By definition, these UBS are the tightest possible bounds that cover every  $f \in \mathcal{H}_{D^{\text{train}}}$  (i.e.,  $\underline{UB}_{\text{pw}}(x) \leq f(x) \leq \overline{UB}_{\text{pw}}(x) \forall x \in X$ ). From a Bayesian perspective, such bounds correspond to credible bounds for  $\alpha = 1$  if the support of the prior is contained in  $\mathcal{H}$ . Interestingly, if  $\mathcal{H}$  is the class of regularized NNs, these bounds can also be interpreted as an approximation of credible bounds for  $\alpha < 1$  with respect to a Gaussian prior on the parameters of a NN (see Appendix A.1. for a derivation).<sup>6</sup>

In applications like BO, when optimizing an acquisition function based on these pointwise-defined bounds, we require the UBS for all  $x \in X$ . Thus, numerically optimizing

<sup>6</sup>Standard BNNs also aim to approximate the posterior coming from exactly this prior.

such an acquisition function is practically infeasible, as it would require solving the optimization problems (6) or (7) millions of times. In NOMU, we circumvent this problem by constructing the UBS for *all*  $x \in X$  simultaneously. We can do so by only solving a *single* optimization problem, i.e., minimizing the NOMU loss from (5).

In the following theorem, we show that these pointwise-defined UBS can be computed by solving a single optimization problem under the following assumption.

**Assumption 1** (UPWARDS DIRECTED) *For every  $f_1, f_2 \in \mathcal{H}_{D^{\text{train}}}$  there exists an  $f \in \mathcal{H}_{D^{\text{train}}}$  such that  $f(x) \geq \max(f_1(x), f_2(x))$  for all  $x \in X$ .*

**Theorem 4.1** (SINGLE OPTIMIZATION PROBLEM) *Let  $X = \prod_{i=1}^d [a_i, b_i] \subset \mathbb{R}^d$ ,  $a_i < b_i$ , let  $Y = \mathbb{R}$ , and let  $D^{\text{train}}$  be a nonempty set of training points. Furthermore, let  $\mathcal{H}_{D^{\text{train}}} \subset (C(X, Y), \|\cdot\|_\infty)$  be compact and upwards directed and  $\hat{f} \in \mathcal{H}_{D^{\text{train}}}$ . Then, for every strictly-increasing and continuous  $u : \mathbb{R} \rightarrow \mathbb{R}$ , it holds that*

$$\overline{UB}_{\text{pw}} = \arg \max_{h \in \mathcal{H}_{D^{\text{train}}}} \int_X u(h(x) - \hat{f}(x)) dx. \quad (8)$$

In words,  $\overline{UB}_{\text{pw}}$  can be calculated via a single optimization problem (8) on  $\mathcal{H}_{D^{\text{train}}}$ .<sup>7</sup> See Appendix A.2. for the proof.<sup>8</sup>

In practice, Assumption 1 can be violated such that a straightforward calculation of the r.h.s. of (8) for an *arbitrary*  $u$  would result in unreasonable UBS. However, for a sensible choice of  $u$ , NOMU's UBS based on the r.h.s. of (8) still satisfy our Desiderata D1–D4, similar to  $\overline{UB}_{\text{pw}}$  (see Appendix A.3. for a discussion).

The result can be intuitively understood, by observing that minimizing NOMU's loss function  $L^\pi$  (Equation (5)) can be interpreted as solving the r.h.s. of (8) for a specific choice of  $u$ , when  $\mathcal{H}$  is the class of regularized NNs. In detail:

- Term (a) of the NOMU-loss (5) implements that  $\hat{f}$  solves the regression task and thus  $\hat{f} \in \mathcal{H}_{D^{\text{train}}}$  up to numerical precision (if the regularization  $\lambda$  is small enough).
- Term (b) enforces  $\hat{f}_f(x_i^{\text{train}}) \approx 0$  and thus when defining  $h := \hat{f} + \hat{f}_f$ , we directly obtain  $h(x_i^{\text{train}}) \approx y_i^{\text{train}}$  corresponding to the constraint  $h \in \mathcal{H}_{D^{\text{train}}}$  in (8).
- While terms (a) and (b) enforce the constraints of (8), term (c) is the objective function of (8) for the specific choice of  $u(z) := -e^{-c_{\text{exp}} z}$ ,  $c_{\text{exp}} \in \mathbb{R}_{\geq 0}$ .

**Remark 4.2** *In Appendix C.2., we present another version of NOMU, specifically designed for settings in which  $\mathcal{H}_{D^{\text{train}}}$  is upwards directed, i.e., fulfills Assumption 1.*

<sup>7</sup>We formulate Theorem 4.1 for upper UBS  $\overline{UB}_{\text{pw}}$ . The analogous statement also holds for lower UBS  $UB_{\text{pw}}$ .

<sup>8</sup>In Appendix A.2., we prove and state an even more general theorem, in particular allowing for a more general choice of  $X$ .

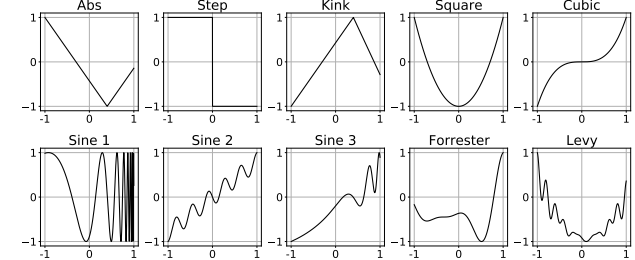


Figure 3. 1D synthetic test functions.

## 5. Experimental Evaluation

In this section, we experimentally evaluate NOMU on synthetic and real data. We first consider 1D and 2D regression tasks, before moving on to Bayesian optimization tasks with up to 20-dimensional input. We compare NOMU with three benchmarks, each of which gives a mean  $\hat{f}(x)$  and model uncertainty prediction  $\hat{\sigma}_f(x)$  (see Appendix B.1. for detailed formulas). Model-specific UBS at  $x \in X$  are given by  $(\hat{f}(x) \mp c \hat{\sigma}_f(x))$  with calibration parameter  $c \in \mathbb{R}_{\geq 0}$ . We then use these UBS when evaluating all methods. We release our code under an open-source license at: [www.github.com/marketdesignresearch/NOMU](https://www.github.com/marketdesignresearch/NOMU).

**Benchmarks.** For all experiments, we consider three benchmarks. First, we consider two approaches that are specialized for performing approximate inference for NNs: (i) MC dropout (MCDO), and (ii) deep ensembles (DE). As a reference point, we also include a non-NN-based benchmark: (iii) Gaussian process (GP) with RBF kernel.

### 5.1. Regression

To develop some intuition, we first study the UBS of all methods using a set of synthetic real-valued test functions with one-dimensional input. In Appendix B.2.3, we provide results for 2D regression.

**Experiment Setup.** We consider ten different synthetic 1D functions whose graphs are shown in Figure 3. The test function battery includes non-differentiable functions, oscillating functions with constant and increasing frequencies including drift components, and smooth polynomials. Moreover, we consider the two popular benchmark functions Levy and Forrester, which have multiple local optima.<sup>9</sup> For each test function, we conduct 500 runs. In each run, we randomly sample eight input training points from the input space  $X := [-1, 1]$  without adding data noise, such that

<sup>9</sup>[www.sfu.ca/~ssurjano/optimization.html](http://www.sfu.ca/~ssurjano/optimization.html) All test functions are shifted and scaled to  $X=[-1, 1]$  and  $f(X) = [-1, 1]$ .

the only source of uncertainty is model uncertainty.<sup>10</sup> For each run, we also generate 100 *validation points* in the same fashion, which we then use to assess the quality of the UBS.

**NOMU Setup.** For NOMU, for each of the two sub-networks, we use a standard feedforward NN with three fully connected hidden layers à  $2^{10}$  nodes, ReLU activations and hyperparameters  $\pi_{\text{exp}} = 0.01$ ,  $\pi_{\text{sq}} = 0.1$ ,  $c_{\text{exp}} = 30$ . Moreover, we set  $\lambda = 10^{-8}$  accounting for very small data-noise,  $\ell_{\text{min}} = 0.001$  and  $\ell_{\text{max}} = 2$ , where the latter can be seen as deciding for a prior standard deviation equal to 2.

To enable a fair comparison of all methods, we use generic representatives of all methods and do not optimize any of them for any test function. Furthermore, we choose the architectures of all NN-based methods, such that the overall number of parameters is comparable. We provide all methods with the same prior information (specifically, this entails knowledge of zero data noise), and we set the corresponding parameters accordingly. Finally, we set all remaining hyperparameters of the benchmarks to the default values proposed in the respective literature. For details regarding the configurations of the benchmarks, please see Appendix B.2.1.

### 5.1.1. PERFORMANCE MEASURES

Following prior work (Khosravi et al., 2010; Pearce et al., 2018), we measure the quality of all UBS by contrasting their *mean width* (*MW*) (i.e., the average width of the UBS at a set of validation points  $D^{\text{val}}$ ) with their *coverage probability* (*CP*) (i.e., the proportion of points from  $D^{\text{val}}$  that are covered by the UBS). Ideally, *MW* should be as small as possible, while *CP* should be close to its maximal value 1. Clearly, *CP* is counter-acting *MW*. This naturally motivates considering ROC-like curves, plotting *MW* against *CP* for a range of calibration parameters  $c$ , and comparing different UBS based on their *area under the curves* (termed *AUC* in this paper). Additionally, we report the widely used *average negative log (Gaussian) predictive density* (*NLPD*), minimized over the calibration parameter  $c$ , which we denote as  $\text{NLPD}_{\text{min}}$  (Quinonero-Candela et al., 2005; Lakshminarayanan et al., 2017; Pearce et al., 2018). We refer to Appendix B.2.2. for further details.

### 5.1.2. SYNTHETIC FUNCTIONS RESULTS

In Table 1, we present median values of *AUC* and  $\text{NLPD}_{\text{min}}$  across all 5000 runs (500 runs for 10 test functions) for each algorithm. We also provide a 95% bootstrap confidence interval (CI) to assess statistical significance. We see that NOMU performs well on both measures and yields numbers similar to those of DE. The GP is only competitive on  $\text{NLPD}_{\text{min}}$ . MCDO performs worst for both measures.

<sup>10</sup>We choose a small number of training points for this experiment s.t. the characteristics of the different UBS are clearly visible.

MODEL	AUC	$\text{NLPD}_{\text{MIN}}$
NOMU	0.21 [0.21, 0.22]	-1.76 [-1.81, -1.72]
GP	0.45 [0.41, 0.50]	-1.77 [-1.89, -1.67]
MCDO	0.30 [0.29, 0.30]	-1.02 [-1.05, -0.99]
DE	0.22 [0.21, 0.23]	-1.75 [-1.79, -1.70]

Table 1. Aggregate results for NOMU, GP, MCDO and DE for the set of all ten 1D synthetic functions. Shown are the medians of each measure across all runs. Winners are marked in green.

Table 2 provides a more detailed view, showing the ranks achieved by each algorithm for each individual 1D synthetic function (see Appendix B.2.3 for corresponding measures). For each function, we calculate the ranks based on the medians and a 95% bootstrap CI. An algorithm loses one rank to each other algorithm that significantly dominates it. We observe that NOMU is the only algorithm that never comes in third or fourth place. Thus, while some algorithms do particularly well in capturing uncertainties of functions with certain characteristics (e.g. RBF-GPs for polynomials), NOMU is the only algorithm that consistently performs well.

For 2D regression, we provide results and visualizations of the UBS in Appendix B.2.3. and B.2.4. We observe similar performance and characteristics of the different algorithms.

**UB Characteristics.** We have investigated the *shape* of the UBS produced by all algorithms for all ten 1D functions. Figure 4 exemplifies our findings, showing typical UBS for the Levy test function as obtained in one run. In Appendix B.2.4., we provide visualisations for other test functions.

We find that MC dropout consistently yields tube-like UBS; in particular, its UBS do not narrow at training points. Moreover, it only fulfills D3 (Out-of-Sample) to a limited degree.

We frequently observe that DE leads to UBS of somewhat arbitrary shapes. This can be seen most prominently in Figure 4 around  $x \approx -0.8$  and at the edges of its input

FUNCTION	NOMU	GP	MCDO	DE
ABS	1,1	3,3	3,4	1,1
STEP	2,2	4,4	2,3	1,1
KINK	1,1	3,3	3,4	1,1
SQUARE	2,2	1,1	4,4	2,3
CUBIC	2,2	1,1	3,4	3,3
SINE 1	2,1	4,1	1,1	2,1
SINE 2	2,1	4,2	1,2	3,3
SINE 3	1,1	4,1	3,4	1,1
FORRESTER	2,2	1,1	3,4	3,3
LEVY	1,1	4,4	1,3	3,1

Table 2. Detailed results for NOMU, GP, MCDO and DE, for all ten 1D synthetic functions. Shown are ranks (1=best to 4=worst) according to the medians for the two measures AUC (listed first) and  $\text{NLPD}_{\text{min}}$  (listed second). Winners are marked in green.

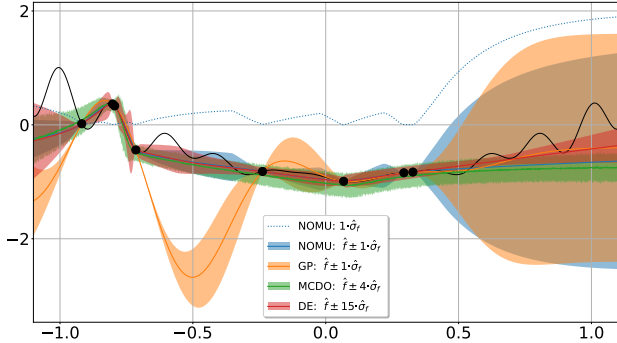


Figure 4. UBs resulting from NOMU, GP, MCDO and DE for the Levy function (solid black line). For NOMU, we additionally show  $\hat{\sigma}_f$  as a dotted blue line. Training points are shown as black dots.

range, where DE's UBs are very different in width with no clear justification. In addition, we sometimes see that also DE's UBs do not narrow sufficiently at training points.

In contrast, NOMU displays the behaviour it is designed to show. Its UBs nicely tighten at training points and expand in-between (**D1–D3**, for **D4 (Metric Learning)** see Appendix A.4). Furthermore, Figure 4 shows how  $\ell_{\max}$  realizes as maximal prior uncertainty.

The quality of the GP's UBs varies with the test function. Figure 4 shows an instance in which the GP's mean predictions overshoots at  $x = -0.5$ , although the RBF-kernel is a reasonable choice for the  $C^\infty$ -Levy function.

### 5.1.3. RESULTS FOR A REAL DATA TIME SERIES

Next, we consider the popular benchmark of interpolating the reconstructed solar irradiance data set also studied in [Gal & Ghahramani \(2016\)](#).<sup>11</sup> We split the data set (scaled to  $X = [-1, 1]$ ) into 194 training and 197 validation points. As in [Gal & Ghahramani \(2016\)](#), we choose five intervals to contain only validation points.<sup>12</sup>

Figure 5 visualizes the UBs obtained by NOMU. We observe that NOMU manages to fit the training data while capturing model uncertainty in-between input training points. In particular, interpolation regions are successfully modeled as regions of high model uncertainty. The respective plots for the benchmarks as well as the performance measures are provided in Appendix B.2.5. There, we observe the same patterns as in the synthetic setting: MCDO does not narrow at training points, DE displays somewhat arbitrary behavior, and GP’s mean prediction is overshooting.

## 5.2. Bayesian Optimization

Analyzing the regression setting has provided us with a good view on the typical UB characteristics. Ultimately, however, we are interested in assessing the performance of NOMU in high-dimensional *Bayesian optimization (BO) tasks*, which is a particularly important application (Frazier, 2018).

**Experiment Setup.** In BO, the goal is to maximize an unknown expensive-to-evaluate function, given a budget of function queries. We use a battery of synthetic test functions with different characteristics from the same library as before, but now in 5 to 20 dimensions  $d$ , transformed to  $X = [-1, 1]^d$ ,  $f(X) = [-1, 1]$ .<sup>13</sup> For each test function, we randomly sample 8 initial points  $(x_i, f(x_i))$  and let each algorithm choose 64 further function evaluations (one by one) using its upper UB as acquisition function. This corresponds to a setting where one can only afford 72 expensive function evaluations in total.<sup>14</sup> We provide details regarding the selected hyperparameters for each algorithm in Appendix B.3.1. We measure the performance of each algorithm based on its *final regret*  $|\max_{x \in X} f(x) - \max_{i \in \{1, \dots, 72\}} f(x_i)| \in [0, 2]$ .

Recall that, for each algorithm, the UBS must be calibrated by choosing appropriate values for the parameter  $c$ . For each algorithm, we do so in the following straightforward way. First, after observing the 8 random initial points, we determine those two values of  $c$  for which the resulting mean width (MW) of the UBS is 0.05 and 0.5, respectively (we call this MW SCALING).<sup>15</sup> We perform one BO run for both resulting initial values for  $c$ . Additionally, if in the course of a BO run, an algorithm were to choose an input point  $x_i$  very close to an already observed point  $x_i$ , we increase  $c$  dynamically to make it select a different input point instead (we call this DYNAMIC C; see Appendix B.3.2. for details). Given the function range, a value of 0.05 in MW SCALING corresponds to small model uncertainty, such that exploration is mainly due to DYNAMIC C. Smaller values than 0.05 therefore lead to similar outcomes. In contrast, a value of 0.5 corresponds to large model uncertainties, such that DYNAMIC C is rarely used. Only for the “plain GP (pGP)” algorithm do we not use MW SCALING nor DYNAMIC C, as pGP uses its default calibration ( $c$  is determined by the built-in hyperparameter optimization in every step). However, a comparison of GP and pGP by the mean final regrets (across all functions) suggests that MW SCALING and DYNAMIC C surpass the built-in calibration (see Table 3). As a baseline,

<sup>11</sup>The data is taken from (Steinhilber et al., 2009).

<sup>12</sup> After inspecting the training data, we decided (a priori) that the underlying function is likely of high frequency. Therefore, we set  $\lambda = 10^{-10}$  for NOMU, and we set the benchmarks' regularization accordingly. Moreover, we set  $\pi_{\text{exp}} = 0.05$ ,  $\ell_{\text{min}} = 0.01$  to account for small non-zero data noise.

<sup>13</sup>These test functions are designed for minimization. Thus, for our experiments, we multiply each test function by  $-1$  and equivalently maximize them instead.

<sup>14</sup>We also ran simulations with 100 random initial points and 64 BO steps. However, this did not lead to an improvement.

<sup>15</sup>We chose two values of MW instead of  $c$ , since the scales of the different algorithms varies by multiple orders of magnitude.

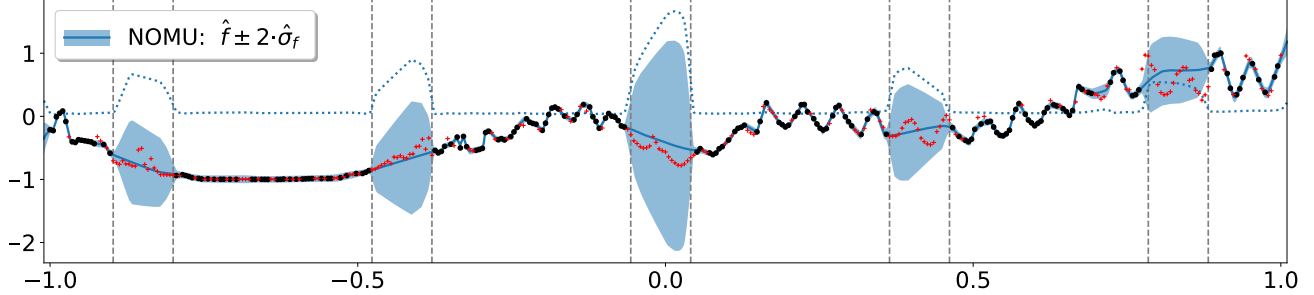


Figure 5. Visualization of NOMU’s model prediction (solid blue line) and UBs (shaded blue area) on the solar irradiance data set. Training and validation points are shown as black dots and red crosses, respectively. NOMU’s model uncertainty is shown as a dotted line.

we also consider random search (RAND).

**Results.** In Table 3, we present the BO results for four 5D functions, four 10D functions, and four 20D functions. We show the average final regret achieved across the four functions per dimension; additionally, we show the ranks achieved by each algorithm for each individual function. For each algorithm and dimension, we give the results corresponding to the MW scaling parameter (0.05 or 0.5) that minimizes the average final regret across that dimension (see Appendix B.3.3. for both MWs). In practice, one often only knows the dimensionality of a given BO task, which is why we use the average final regret per dimension as the criterion for picking the optimal scaling parameter.

In Table 3, we see that NOMU outperforms all other benchmarks in terms of average final regret, for each dimension. By inspecting the ranks achieved for each individual function, we further observe that NOMU is always ranked 1<sup>st</sup> or 2<sup>nd</sup>. In contrast, the performance of the benchmarks heavily depends on the test function; and each benchmark is ranked

FUNCTION	NOMU	GP	MCDO	DE	pGP	RAND
GFUNCTION5D	2	5	1	3	3	6
LEVY5D	1	3	4	2	4	6
PERM5D	2	6	1	3	2	4
ROSENROCK5D	1	3	2	1	3	6
<i>Average Regret 5D</i>	<b>0.03</b>	0.12	0.09	0.06	0.16	0.38
GFUNCTION10D	2	4	1	2	4	6
LEVY10D	1	1	5	2	3	6
PERM10D	2	3	2	4	2	1
ROSENROCK10D	1	4	1	5	1	6
<i>Average Regret 10D</i>	<b>0.10</b>	0.16	0.25	0.13	0.20	0.45
GFUNCTION20D	1	5	4	1	2	5
LEVY20D	1	1	5	4	3	6
PERM20D	2	2	2	3	2	1
ROSENROCK20D	1	4	1	6	3	5
<i>Average Regret 20D</i>	<b>0.16</b>	0.19	0.44	0.27	0.22	0.48

Table 3. Results for 12 different BO tasks. Shown are the average final regrets per dimension and the ranks for each individual function (1=best to 6=worst), based on the final regret and a 95% CI over 100 (5D) and 50 (10-20D) runs. Winners are marked in green.

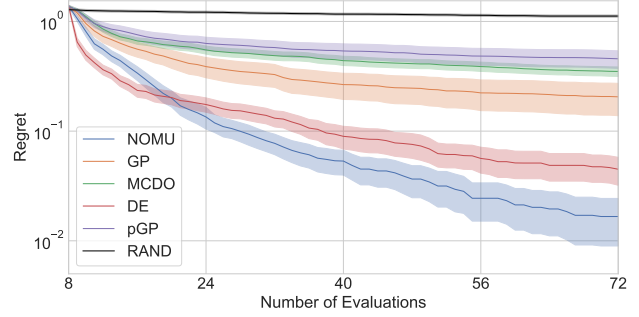


Figure 6. Regret plot for Levy5D. For each BO step, we show the regrets averaged over 100 runs (solid lines) with 95% CIs.

4<sup>th</sup>, 5<sup>th</sup>, or 6<sup>th</sup> multiple times.

For Perm10D and Perm20D we see that RAND performs best. However, due to a flat optimum of these functions, all algorithms achieve similar (very small) final regrets of 1e-3 to 1e-5 for all dimensions (see Appendix B.3.3.).

In Figure 6, we present the regret plot for Levy5D. We see that NOMU significantly outperforms all other algorithms. See Appendix B.3.4. for regret plots for all functions.

## 6. Conclusion

In this paper, we have introduced a new algorithm for estimating model uncertainty for NNs, which we call *neural optimization based model uncertainty (NOMU)*. NOMU can estimate model uncertainty for any given previously trained NN, if given access to its training data. By using a carefully-designed loss function, we have ensured that the resulting UBs satisfy four important desiderata regarding model uncertainty. For regression, our experimental results show that NOMU performs as good or better than state-of-the-art methods on a wide variety of synthetic test functions. For higher-dimensional BO tasks, our results show that NOMU significantly outperforms all considered benchmarks.

---

We see great potential to further improve NOMU, for example by choosing a different  $u$  or  $\varphi$ , or by modifying the architecture (e.g., different connections between the mean and uncertainty sub-networks, or different regularization of certain connections). We also envision several extensions of NOMU, including its application to classification, employing different architectures (CNNs, RNNs, or Transformers), and incorporating data noise. Finally, it would be interesting future work to study the application of NOMU to reinforcement learning and active learning tasks.

## Acknowledgements

We thank Marius Högger for insightful discussions and his excellent research assistance in implementing the Bayesian optimization experiments. This paper is part of a project that has received funding from the European Research Council (ERC) under the European Union’s Horizon 2020 research and innovation programme (Grant agreement No. 805542).

## Appendix

### A. Theoretical Analysis

In this section, we first briefly discuss why  $\underline{UB}_{\text{pw}}$ ,  $\overline{UB}_{\text{pw}}$  are desirable and elaborate on *relative uncertainties* (Appendix A.1). Then, we prove Theorem 4.1 (Appendix A.2). Finally, we discuss the case if  $\mathcal{H}_{D^{\text{train}}}$  is not *upwards directed* as assumed in Theorem 4.1 and further show how we deal with this challenge (Appendix A.3).

In the following, we denote by  $\mathcal{NN}_{\theta}^f : X \rightarrow Y$  a (standard) NN for model predictions. Note that  $\mathcal{NN}_{\theta}^f$  does not represent the whole NOMU architecture but can be used as  $\hat{f}$ -sub-network in the NOMU architecture  $\mathcal{NN}_{\theta}$ .

#### A.1. Pointwise Uncertainty Bounds: $\underline{UB}_{\text{pw}}$ , $\overline{UB}_{\text{pw}}$

In this paper, we consider the hypothesis class of regularized NNs, i.e.,  $\mathcal{H} := \{\mathcal{NN}_{\theta}^f : \|\theta\|_2 \leq \gamma\}$ . Recall that one needs to assume that the prior is fully concentrated on  $\mathcal{H}$  in order to interpret the pointwise UBS  $\underline{UB}_{\text{pw}}$ ,  $\overline{UB}_{\text{pw}}$  as  $\alpha=1$  CBs. In the following, we will present an alternative Bayesian interpretation of  $\overline{UB}_{\text{pw}}$ .

Many other approaches (MC dropout, BNNs) assume a Gaussian prior on the parameters of the NNs, i.e.,  $\theta \sim \mathcal{N}(0, \sigma_{\theta}^2 I)$ , and try to approximate the corresponding posterior CBs. Interestingly,  $\underline{UB}_{\text{pw}}$  and  $\overline{UB}_{\text{pw}}$  can also be seen as approximations of  $\alpha < 1$  credible bounds in the case of such a Gaussian prior on the parameters. This can be seen as follows:

Let the data generating process be given as  $y = \mathcal{NN}_{\theta}^f + \varepsilon$ , with  $\varepsilon \sim \mathcal{N}(0, \sigma_{\text{n}}^2)$  (i.e., in this section, for simplicity we assume homoskedastic noise). For a Gaussian prior on the parameters  $\theta \sim \mathcal{N}(0, \sigma_{\theta}^2 I)$  the negative log posterior can be written as

$$\begin{aligned} -\log(p(\theta|D^{\text{train}})) &= \underbrace{\frac{1}{2\sigma_{\text{n}}^2} \sum_{i=1}^{n^{\text{train}}} (\mathcal{NN}_{\theta}^f(x_i^{\text{train}}) - y_i^{\text{train}})^2}_{=: L(\theta)} \\ &+ \frac{\|\theta\|_2^2}{2\sigma_{\theta}^2} + n^{\text{train}} \log(\sigma_{\text{n}}) + C_{n^{\text{train}}, \sigma_{\theta}}. \end{aligned} \quad (9)$$

for a constant  $C_{n^{\text{train}}, \sigma_{\theta}} := \frac{n^{\text{train}}}{2} \log(2\pi) + \frac{1}{2} \log(2\pi\sigma_{\theta}^2)$ . Then the pointwise upper UBS can be reformulated to

$$\overline{UB}_{\text{pw}}(x) \stackrel{\text{def.}}{=} \sup_{f \in \mathcal{H}_{D^{\text{train}}}} f(x) = \lim_{\sigma_{\text{n}} \rightarrow 0} \sup_{f \in \tilde{\mathcal{H}}_{D^{\text{train}}}^{\sigma_{\text{n}}}} f(x) \quad (10)$$

with

$$\tilde{\mathcal{H}}_{D^{\text{train}}}^{\sigma_{\text{n}}} := \left\{ \mathcal{NN}_{\theta}^f : \frac{\sigma_{\theta}^2}{\sigma_{\text{n}}^2} L(\theta) + \|\theta\|_2^2 \leq \gamma \right\} \quad (11a)$$

$$= \left\{ \mathcal{NN}_{\theta}^f : \log(p(\theta|D^{\text{train}})) \geq \tilde{\gamma}_{\sigma_{\text{n}}} \right\} \quad (11b)$$

$$\text{where } \tilde{\gamma}_{\sigma_{\text{n}}} := -\frac{\gamma}{2\sigma_{\theta}^2} - n^{\text{train}} \log(\sigma_{\text{n}}) - C_{n^{\text{train}}, \sigma_{\theta}}.$$

Therefore, for small data noise  $\sigma_{\text{n}} \approx 0$  we obtain from eqs. (10) and (11b) that

$$\overline{UB}_{\text{pw}}(x) \approx \sup_{\theta} \left( \mathcal{NN}_{\theta}^f(x) : p(\theta|D^{\text{train}}) > e^{\tilde{\gamma}_{\sigma_{\text{n}}}} \right). \quad (12)$$

In words, from a Bayesian point of view, we seek the highest value  $\mathcal{NN}_{\theta}^f(x)$  provided that the posterior density  $p(\theta|D^{\text{train}}) > e^{\tilde{\gamma}_{\sigma_{\text{n}}}}$ , which can be seen as a heuristic to approximate CBs similarly as the MAP from the parameter-space is a commonly used heuristic to approximate the posterior mean of  $y$ .

**Remark A.1** Note, that if  $p(\mathcal{NN}_{\theta}^f(x)|D^{\text{train}}) = p(\theta|D^{\text{train}})$  and this posterior is unimodal, (12) corresponds to a *classical* highest posterior density interval (HPDI).

Thus, pointwise UBS can be seen as an alternative method to approximate BNN-based CBs with the typically used Gaussian prior.

**From Absolute to Relative Model Uncertainty.** If the prior scale (e.g.,  $\gamma$  or  $\sigma_{\theta}$  in the above mentioned approaches) is known, in theory no further calibration is needed and one can interpret the resulting UBS in *absolute* terms. However, typically, the prior scale is unknown and the resulting UBS can only be interpreted in terms of *relative* model uncertainty (i.e., how much more uncertainty does one have at one point  $x$  compared to any other point  $x'$ ?) and in a second step careful calibration of the resulting UBS is required.

Thus, there are two (almost) independent problems: First, the fundamental concept of how to estimate relative model uncertainty (such as MC dropout, deep ensembles or NOMU) and second, the calibration of UBS. In this paper, we do not mix up these two challenges and only focus on the first one. Furthermore, all our desiderata and performance measures do not depend on the scaling of the uncertainty.

#### A.2. Proof of Theorem 4.1

In the following, we prove Theorem A.2, an even more general version of Theorem 4.1. The statement of Theorem 4.1 follows from Theorem A.2 by setting

$$1. \quad X \subset \mathbb{R}^d \text{ compact}, Y := \mathbb{R}$$

2.  $\mu = \lambda_d$ , where  $\lambda_d$  is the Lebesgue measure on  $\mathbb{R}^d$  (which is finite on every compact set and has full support).

**Theorem A.2** *Let  $X$  be a nonempty topological space equipped with a finite measure  $\mu$  with full support<sup>16</sup>, let  $Y$  be a normed and totally ordered space and let  $D^{\text{train}}$  denote a set of observations. Moreover, let  $\mathcal{H}_{D^{\text{train}}} \subset (C(X, Y), \|\cdot\|_\infty)$  be compact, and  $\hat{f} \in \mathcal{H}_{D^{\text{train}}}$ . Assume further that  $\mathcal{H}_{D^{\text{train}}}$  is upwards directed (see Assumption 1). Then, for every strictly-increasing and continuous  $u : Y \rightarrow \mathbb{R}$  it holds that*

$$\overline{UB}_{\text{pw}} = \arg \max_{h \in \mathcal{H}_{D^{\text{train}}}} \int_X u(h(x) - \hat{f}(x)) d\mu(x). \quad (13)$$

*Proof.* First note that since  $\mu$  is finite and  $h, \hat{f}$  and  $\overline{UB}_{\text{pw}}$  are bounded since  $\mathcal{H}_{D^{\text{train}}}$  is assumed to be compact with respect to the  $\|\cdot\|_\infty$ -topology, it holds that the integral in (13) is finite.

Let  $h^* \in \mathcal{H}_{D^{\text{train}}}$  denote an optimizer of (13), which exists since  $\mathcal{H}_{D^{\text{train}}}$  is assumed to be compact and the operator  $h \mapsto \int_X u(h(x) - \hat{f}(x)) d\mu(x)$  is continuous on the  $\|\cdot\|_\infty$ -topology.

We want to show that  $h^*(x) = \overline{UB}_{\text{pw}}(x)$  for every  $x \in X$ .

Note that per definition for all  $x \in X$  and  $h \in \mathcal{H}_{D^{\text{train}}}$  it holds that

$$\overline{UB}_{\text{pw}}(x) = \sup_{f \in \mathcal{H}_{D^{\text{train}}}} f(x) \geq h(x). \quad (14)$$

Thus  $\overline{UB}_{\text{pw}}(x) \geq h^*(x)$  for all  $x \in X$ .

For the reverse inequality assume on the contrary that there exists an  $x' \in X$  such that

$$\overline{UB}_{\text{pw}}(x') > h^*(x'). \quad (15)$$

Then, we define  $f_{x'} := \arg \max_{f \in \mathcal{H}_{D^{\text{train}}}} f(x')$ , which exists because of compactness and continuity. Since  $f_{x'}$  and  $h^*$  are both continuous and  $f_{x'}(x') = \overline{UB}_{\text{pw}}(x') > h^*(x')$  there exists a neighbourhood  $U_{x'}$  of  $x'$  such that

$$f_{x'}(x) > h^*(x) \text{ for all } x \in U_{x'}, \quad (16)$$

Using the *upwards directed* property with  $f_1 := f_{x'}$  and  $f_2 := h^*$ , it follows that there exists a  $\tilde{h} \in \mathcal{H}_{D^{\text{train}}}$  with

$$\tilde{h}(x) \geq \max(f_{x'}(x), h^*(x)) \text{ for all } x \in X. \quad (17)$$

Using (16) together with (17) implies further that

$$\tilde{h}(x) \geq h^*(x) \text{ for all } x \in X \text{ and} \quad (18)$$

$$\tilde{h}(x) > h^*(x) \text{ for all } x \in U_{x'}. \quad (19)$$

However, since  $u$  is strictly increasing and  $\mu(U_{x'}) > 0$  by the full support assumption, we get that

$$\int_X u(\tilde{h}(x) - \hat{f}(x)) d\mu(x) > \int_X u(h^*(x) - \hat{f}(x)) d\mu(x), \quad (20)$$

which is a contradiction to the assumption that  $h^*$  is the optimizer of (13). Therefore, it holds that  $\overline{UB}_{\text{pw}}(x) \leq h^*(x)$  for all  $x \in X$ .

In total we get that  $\overline{UB}_{\text{pw}}(x) = h^*(x)$  for all  $x \in X$ , which concludes the proof.  $\square$

**Discussion of Assumptions.** For our algorithm we select  $\mathcal{H} := \left\{ \mathcal{NN}_\theta^f : \|\theta\|_2 \leq \gamma \right\}$  to be the class of regularized NNs with a continuous activation function. Thus, the assumption of  $\mathcal{H}_{D^{\text{train}}}$  being compact and a subset of  $C(X, Y)$  is fulfilled. In the following section we discuss Assumption 1.

### A.3. A Note on Theorem 4.1

In practice, the set  $\mathcal{H}_{D^{\text{train}}}$  often is not upwards directed for typical NN-architectures and Equation (8) of Theorem 4.1 is not fulfilled in general (see Appendix C.2 for a specifically designed version of NOMU if  $\mathcal{H}_{D^{\text{train}}}$  is upwards directed). Indeed,  $h^* := \arg \max_{h \in \mathcal{H}_{D^{\text{train}}}} \int_X u(h(x) - \hat{f}(x)) d\mu(x)$  can be much more overconfident than  $\overline{UB}_{\text{pw}}$ . However, in the following we will motivate why for a suitably chosen  $u$  the relative model uncertainty of  $h^*$  still fulfills the desiderata D1 (Non-Negativity), D2 (In-Sample) and D3 (Out-of-Sample).

**Remark A.3** *In our proposed final algorithm from Section 3 NOMU, we incorporated D4 (Metric Learning) by modifying the network architecture as presented in Section 3.2.*

**Problem.** First, we give an example of a specific NN-architecture, where Theorem 4.1 is not fulfilled due to a violation of the upwards directed assumption. Note that from a Lagrangian perspective it is equivalent to add a term  $-\lambda \|\theta\|_2^2, \lambda \geq 0$  to the target function of (8) instead of bounding  $\|\theta\|_2^2 \leq \gamma^2$  as a constraint in  $\mathcal{H}_{D^{\text{train}}}$ . Moreover, for a specific NN-architecture it is shown that regularizing  $\|\theta\|_2^2$  is equivalent to regularizing the  $L_2$ -norm of the second derivative of the function  $f = \mathcal{NN}_\theta^f$  (Heiss et al., 2019), i.e., regularizing  $\int_X f''(x)^2 dx$ . If we choose for example  $u = id : \mathbb{R} \rightarrow \mathbb{R}$ , then increasing  $h$  in-between the two close points in the middle of Figure 7, would improve the target function of (8)  $\int u(h(x) - \hat{f}(x)) dx$  less than the additional regularization cost resulting from the additional second derivative when increasing  $h$ . Therefore,  $h^*$  will be below the mean prediction  $\hat{f}$  in this region, break D1 (Non-Negativity), and  $h^* \neq \overline{UB}_{\text{pw}}$ .

**Solution.** However, if e.g., we choose  $u : x \mapsto -e^{-c_{\text{exp}}x}$  with  $c_{\text{exp}}$  large enough, we highly penalize  $h < \hat{f}$ , and

<sup>16</sup>I.e. every nonempty open set has non-zero measure.

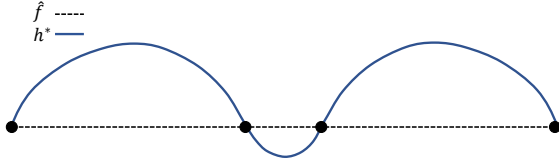


Figure 7.  $h^*$  would not fulfill **D1 (Non-Negativity)**, if  $u$  was chosen as the identity and the architecture from Heiss et al. (2019) was used.

thus  $\hat{f} \leq h^*$  **D1 (Non-Negativity)** is fulfilled. Since  $h^* \in \mathcal{H}_{D\text{train}}$ , it follows that  $h^*(x_i^{\text{train}}) - \hat{f}(x_i^{\text{train}}) = 0$  for all training points. This together with  $\hat{f} \leq h^*$  implies that  $\nabla(h^* - \hat{f})(x_i^{\text{train}}) = 0$  at the training points (in the interior of  $X$ ), which subsequently interrupts the downwards trend of  $h^* - \hat{f}$  from one side of a point to the other side of a point as depicted in Figure 8.

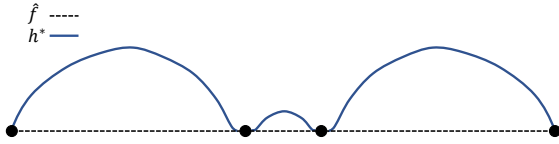


Figure 8.  $h^*$  fulfills **D1–D3** if  $u$  prevents it from getting negative.

#### A.4. A Note on Desideratum D4 (Metric Learning)

**1D.** In order to visualize **D4** and show how in the NOMU approach the mean prediction impacts its model uncertainty prediction we conduct the following experiment. We sample 16 *equidistant* noiseless training points of a trend-adjusted version of *Sine 3*. We then train NOMU (hyperparameters are as in Appendix B.2.1 with  $\pi_{\text{sq}} = 0.5$ ,  $\ell_{\min} = 10^{-4}$ , regularization parameter  $10^{-4}$  on the  $\hat{r}_f$ -network, and number of training epochs  $2^{12}$ ) and compute the corresponding UBs. Figure 9 shows that NOMU UBs are wider (cp. the dotted blue line) in those areas of the input space where small changes of  $x$  lead to large variation in the target ( $\approx x \geq 0$ ) compared to areas without large variation in the target ( $\approx x \leq 0$ ). This effect is present even though the input training points are sampled from an equidistant grid, and thus isolates the effect of **D4**.

**2D.** Analogously, we visualize **D4** for two-dimensional input by training NOMU on 16 training points sampled on an *equidistant*  $4 \times 4$ -grid and evaluated at the two-dimensional extension of the *Step* function, i.e.,

$$f = \mathbb{R}^2 \rightarrow \mathbb{R} : (x_1, x_2) \mapsto \begin{cases} -1 & \text{if } x_1 < 0 \\ 1 & \text{if } x_1 \geq 0. \end{cases} \quad (21)$$

Here, **D4** can be interpreted as follows: imagine we do not have any prior knowledge of whether  $x_1$  or  $x_2$  is more

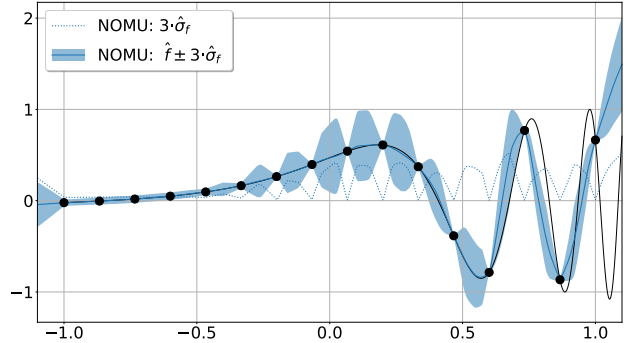


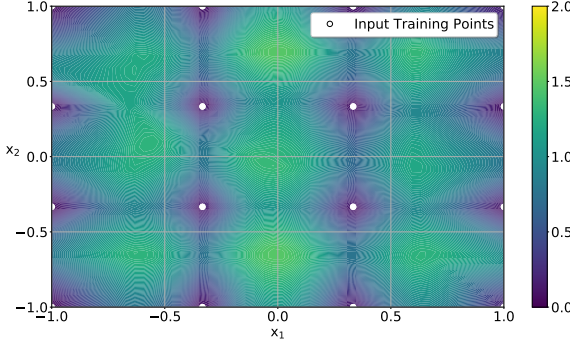
Figure 9. Visualisation of **D4 (Metric Learning)**.

important for predicting the unknown function  $f$ . However, when NOMU observes the 16 training points it should be able to learn that  $x_1$  is more important for the model prediction than  $x_2$ , and that the function behaves more regular/predictable far away from  $\{x_1 \approx 0\}$ . Desideratum **D4** requires in this example that feature  $x_1$  should have a higher impact than feature  $x_2$  also on the model uncertainty prediction. If a model for UBs did not incorporate **D4**, we would expect the uncertainty in this example to fulfill  $\hat{\sigma}_f((x_1, x_2)) = \hat{\sigma}_f((x_2, x_1))$  because of the equidistant grid of the training points (this is indeed the case for GPs, see Figure 11a).

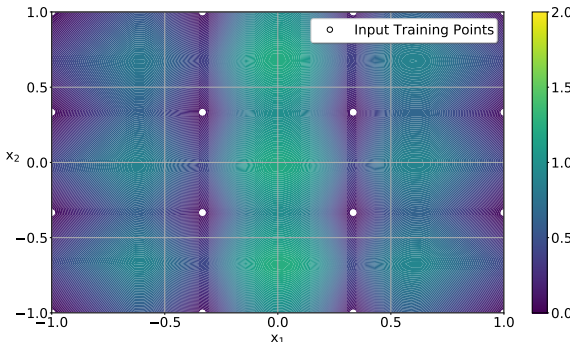
For NOMU however, we have very good control on how strongly we enforce **D4**, e.g., we can strengthen **D4** by increasing the L2-regularization of the hidden layers in the  $\hat{r}_f$ -network and/or decreasing the size of the  $\hat{r}_f$ -network.

In Figure 10, we present the estimated model uncertainty  $\hat{\sigma}_f$  obtained for *different* hyperparameters of the  $\hat{r}_f$ -network with *fixed*  $\hat{f}$ -architecture among all four subplots. Thus, Figure 10 shows how **D4** realizes in different magnitudes. In Figure 10a, we use the same hyperparameters for the  $\hat{r}_f$ -network as for the  $\hat{f}$ -network. In 10b, we only increase the L2-regularization of the  $\hat{r}_f$ -network. In Figure 10c, we only decrease the size of  $\hat{r}_f$ -networks. In Figure 10d, we combine both, i.e., we increase the L2-regularization of the  $\hat{r}_f$ -network and decrease the size of the  $\hat{r}_f$ -network.

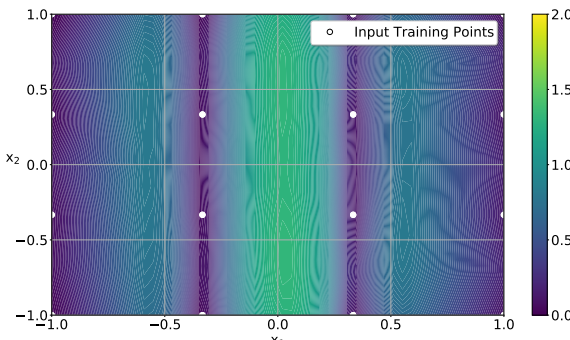
While **D4** is barely visible in Figure 10a, it is clearly visible in Figures 10b–10d. In Figures 10b–10d, we observe that the estimated model uncertainty  $\hat{\sigma}_f$  grows faster in horizontal directions (corresponding to changes in  $x_1$ ) than in vertical directions. In Figures 10b–10d, we further observe that the estimated model uncertainty  $\hat{\sigma}_f$  is larger around  $\{x_1 \approx 0\}$  than far away from this region. The magnitude of both these effects increases from Figure 10b to Figure 10d. Both of these effects can also be observed for MC dropout and deep ensembles (see Figure 11b and Figure 11c).



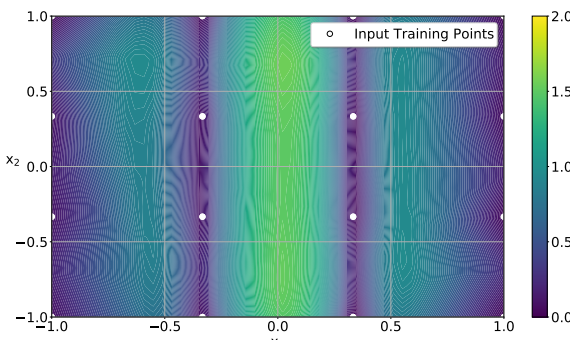
(a) Same L<sub>2</sub>-regularization on the  $\hat{r}_f$ -network and  $\hat{f}$ -network ( $\lambda = 10^{-8}$ ).



(b) Larger L<sub>2</sub>-regularization on the  $\hat{r}_f$ -network ( $\lambda = 10^{-4}$ ) than on the  $\hat{f}$ -network ( $\lambda = 10^{-8}$ ).



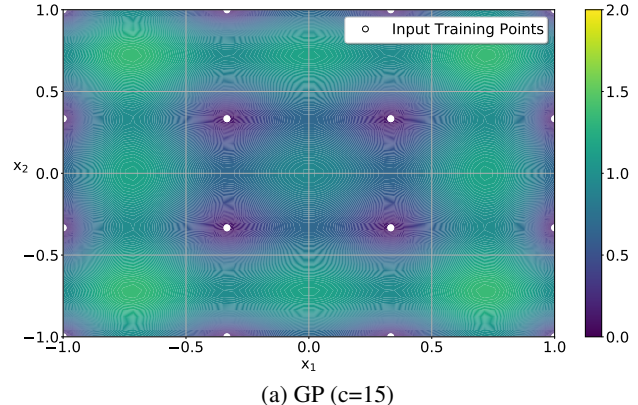
(c) Shallow  $\hat{r}_f$ -network consisting of 4 hidden nodes.



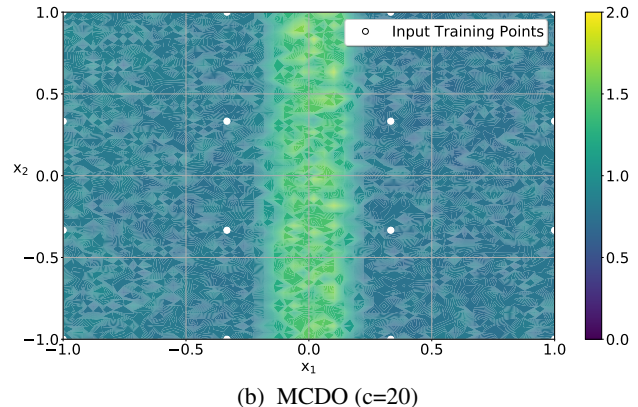
(d) Shallow  $\hat{r}_f$ -network consisting of 4 hidden nodes and larger regularization of  $\lambda = 10^{-4}$  on  $\hat{r}_f$ -network.

Figure 10. Estimated model uncertainty  $\hat{\sigma}_f$  of NOMU: visualizing D4 in 2D.

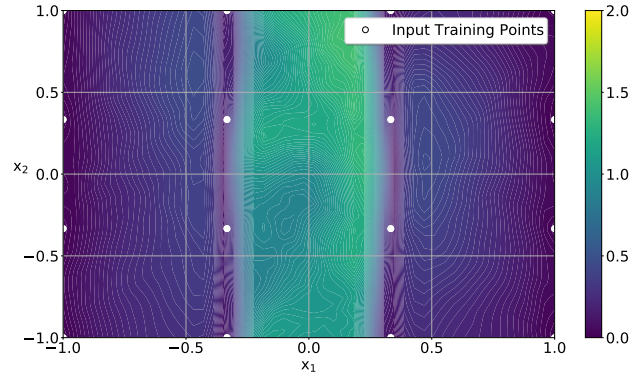
Finally, we present the uncertainty plots of the benchmark methods. We see that deep ensembles give high preference to capturing D4, even though its estimated model uncertainty still is subject to some slight randomness with non-uniform patterns for  $x_1 \in [-0.25, 0.25]$  (Figure 11c). Moreover, MC dropout also captures higher model uncertainty for  $x_1 \in [-0.25, 0.25]$  as desired by D4, but it does not fulfill D2 (Figure 11b). As was expected, the Gaussian process with RBF kernel does not account for D4 (Figure 11a).



(a) GP (c=15)



(b) MCDO (c=20)



(c) DE (c=30)

Figure 11. Estimated model uncertainty of Gaussian process (GP), MC dropout (MCDO) and deep ensembles (DE).

## B. Experiments

### B.1. Benchmark Methods

**Gaussian Process (GP).** A GP defines a distribution over a set of functions  $\{f : X \rightarrow Y\}$  where every finite collection of function evaluations follows a Gaussian distribution (see [Williams & Rasmussen \(2006\)](#) for a survey on GPs). A GP is completely specified by a *mean*  $m : X \rightarrow Y$  and a *kernel* function  $k_\pi : X \times X \rightarrow Y$ , where  $\pi$  denotes a tuple of hyper-parameters. More formally, for any finite set of  $k \in \mathbb{N}$  input points  $\mathbf{x} := \{x_1, \dots, x_k\}$ ,  $x_i \in X$  and for  $\mathbf{f} := (f_1, \dots, f_k) \in Y^k$  with  $f_i := f(x_i)$  it holds that

$$\mathbf{f} \sim \mathcal{N}_k(\mathbf{m}(\mathbf{x}), \mathbf{K}_\pi(\mathbf{x}, \mathbf{x})), \quad (22)$$

i.e., it follows a  $k$ -dimensional Gaussian distribution with covariance (or Gramian) matrix  $[\mathbf{K}_\pi(\mathbf{x}, \mathbf{x})]_{i,j} := k_\pi(x_i, x_j)$ , and mean vector  $\mathbf{m}(\mathbf{x}) := (m(x_1), \dots, m(x_k))$ . Let

$$f \sim \mathcal{GP}(m(\cdot), k_\pi(\cdot, \cdot)), \quad (23)$$

denote a GP with mean function  $m$  and kernel  $k_\pi$ .

In the following, we summarize the main steps of GP regression for a 1D-setting and  $m \equiv 0$ .

1. *Define probabilistic model:*

$$y = f(x) + \varepsilon. \quad (24)$$

2. *Specify prior (kernel and data noise):*

$$f \sim \mathcal{GP}(0, k_\pi(\cdot, \cdot)), \quad (25)$$

$$\varepsilon | \mathbf{x} \sim \mathcal{N}(0, \sigma_n^2(x)). \quad (26)$$

3. *Calculate likelihood* for training points  $\mathbf{x}$  and  $\mathbf{y} := \{y_1, \dots, y_k\}$ :

$$\mathbf{y} | \mathbf{x}, \pi \sim \mathcal{N}_k(\mathbf{0}, \mathbf{K}_\pi(\mathbf{x}, \mathbf{x}) + \text{diag}(\sigma_n^2(\mathbf{x}))), \quad (27)$$

with  $\sigma_n^2(\mathbf{x}) := (\sigma_n^2(x_1), \dots, \sigma_n^2(x_k))$ .

4. *Optimize kernel hyper-parameters (optional):*

$$\hat{\pi} \in \arg \max_{\pi} p(\mathbf{y} | \mathbf{x}, \pi). \quad (28)$$

5. *Calculate posterior predictive distribution* for new point  $(x^*, y^*)$ :

$$y^* | x^*, \mathbf{y}, \mathbf{x}, \hat{\pi} \sim \mathcal{N}(\hat{\mu}(x^*), \hat{\sigma}^2(x^*)), \quad (29)$$

where for  $A := (\mathbf{K}_{\hat{\pi}}(\mathbf{x}, \mathbf{x}) + \text{diag}(\sigma_n^2(\mathbf{x})))$  and  $\mathbf{k}_{\hat{\pi}}(x^*, \mathbf{x}) := (k_{\hat{\pi}}(x^*, x_1), \dots, k_{\hat{\pi}}(x^*, x_k))$  the parameters are given as

$$\hat{\mu}(x^*) := \mathbf{k}_{\hat{\pi}}(x^*, \mathbf{x}) A^{-1} f(\mathbf{x}) \quad (30)$$

$$\hat{\sigma}^2(x^*) := k_{\hat{\pi}}(x^*, x^*) - \mathbf{k}_{\hat{\pi}}(x^*, \mathbf{x}) A^{-1} \mathbf{k}_{\hat{\pi}}(x^*, \mathbf{x})^T. \quad (31)$$

Setting the data noise to zero  $\sigma_n \equiv 0$  in (30) and (31) yields the mean prediction  $\hat{f}$  and the model uncertainty prediction  $\hat{\sigma}_f^2$  as

$$\hat{f}(x^*) = \mathbf{k}_{\hat{\pi}}(x^*, \mathbf{x}) (\mathbf{K}_{\hat{\pi}}(\mathbf{x}, \mathbf{x}))^{-1} f(\mathbf{x}), \quad (32)$$

$$\hat{\sigma}_f^2(x^*) = k_{\hat{\pi}}(x^*, x^*) - \mathbf{k}_{\hat{\pi}}(x^*, \mathbf{x}) (\mathbf{K}_{\hat{\pi}}(\mathbf{x}, \mathbf{x})) \mathbf{k}_{\hat{\pi}}(x^*, \mathbf{x})^T, \quad (33)$$

which are then used to define the Gaussian process's UBs by  $(\hat{f}(x) \mp c \hat{\sigma}_f(x))$  with a calibration parameter  $c \in \mathbb{R}_{\geq 0}$ .

**MC Dropout.** Let  $\mathcal{NN}_\theta^f = W^K \circ \phi \circ W^{K-1} \circ \dots \circ \phi \circ W^1(x)$  be an NN with  $K-1$  hidden layers, activation function  $\phi$ , and fixed parameters  $\theta = \{W^1, \dots, W^K\}$ , which have been trained with added dropout regularization. Furthermore, let  $(p_1, \dots, p_K)$  denote the dropout probability vector used when training  $\mathcal{NN}_\theta^f$ , i.e.,  $p_i$  determines the probability for a single node in the  $i^{\text{th}}$  hidden layer  $W^i$  to be dropped in each backpropagation step.<sup>17</sup>

To obtain model uncertainty one draws  $M$  different NNs according to the dropout probability vector and represents model uncertainty using sample estimates of the mean and variance of the model predictions.<sup>18</sup> These predictions are frequently termed *stochastic forward passes*. More formally, given a dropout probability vector  $(p_1, \dots, p_K)$ , one draws  $M$  realisations  $\{\theta^{(1)}, \dots, \theta^{(M)}\}$  of parameters  $\theta$ , where  $\theta^{(m)} := \{W^{1,(m)}, \dots, W^{K,(m)}\}$ .  $W^{k,(m)}$  is obtained from the original hidden layer  $W^k$  by dropping each column with probability  $p_i$ , i.e., for  $W^k \in \mathbb{R}^{d_{\text{row}} \times d_{\text{col}}}$  set

$$W^{k,(m)} = W^k [z_1^{(m)}, \dots, z_{d_{\text{col}}}^{(m)}], z_j^{(m)} \in \mathbb{R}^{d_{\text{row}}} \quad (34)$$

$$\text{where } z_j^{(m)} := \begin{cases} 0, & \text{with probability } p_i \\ 1, & \text{with probability } 1 - p_i. \end{cases} \quad (35)$$

UBs that represent model uncertainty and *known* data noise  $\sigma_n^2$  are then estimated for each  $x \in X$  as

$$\hat{f}(x) := \frac{1}{M} \sum_{m=1}^M \mathcal{NN}_{\theta^{(m)}}^f(x), \quad (36)$$

$$\hat{\sigma}^2(x) := \underbrace{\frac{1}{M} \sum_{m=1}^M \left( \mathcal{NN}_{\theta^{(m)}}^f(x) - \hat{f}(x) \right)^2}_{\text{model uncertainty}} + \underbrace{\sigma_n^2(x)}_{\text{data noise}}. \quad (37)$$

Setting the data noise to zero  $\sigma_n \equiv 0$  in (37) yields the model uncertainty prediction  $\hat{\sigma}_f^2$  as

$$\hat{\sigma}_f^2(x) := \frac{1}{M} \sum_{m=1}^M \left( \mathcal{NN}_{\theta^{(m)}}^f(x) - \hat{f}(x) \right)^2 \quad (38)$$

<sup>17</sup>One could also use different probabilities  $p_{ij}$  for each node within a hidden layer. The equations extend straightforwardly.

<sup>18</sup>Alternatively, one could also determine the UBs using empirical upper and lower quantiles of the different model predictions.

which defines Mc dropout's UBS as  $\left(\hat{f}(x) \mp c \hat{\sigma}_f(x)\right)$  with a calibration parameter  $c \in \mathbb{R}_{\geq 0}$ .

**Deep Ensembles.** Deep ensembles consists of the following two steps:<sup>19</sup>

1. Use a NN to define a predictive distribution  $p_\theta(y|x)$ , select a pointwise loss function (proper scoring rule)  $\ell(p_\theta, (x, y))$ , which measures the quality of the predictive distribution  $p_\theta(y|x)$  for an observation  $(x, y)$  and define the empirical loss used for training as

$$L(\theta) := \sum_{(x, y) \in D^{\text{train}}} \ell(p_\theta, (x, y)). \quad (39)$$

2. Use an ensemble of NNs, each with different randomly initialized parameters to represent model uncertainty.

Concretely, for regression, Lakshminarayanan et al. (2017) use a NN  $\mathcal{NN}_\theta^f$  with two outputs:  $\hat{\mu}^\theta$  (mean prediction) and  $\hat{\sigma}_n^\theta$  (data noise prediction) and train it using as pointwise loss function the Gaussian negative log-likelihood, i.e.,

$$p_\theta(y|x) := \mathcal{N}\left(y; \hat{\mu}^\theta(x), (\hat{\sigma}_n^\theta(x))^2\right), \quad (40)$$

$$\ell(p_\theta, (x, y)) := \frac{\log\left((\hat{\sigma}_n^\theta(x))^2\right)}{2} + \frac{(\hat{\mu}^\theta(x) - y)^2}{2(\hat{\sigma}_n^\theta(x))^2}. \quad (41)$$

To add model uncertainty, Lakshminarayanan et al. (2017) use an ensemble of  $M$  NNs  $\{\mathcal{NN}_{\theta^{(1)}}^f, \dots, \mathcal{NN}_{\theta^{(M)}}^f\}$ , where each NN outputs a mean and data noise prediction, i.e., for  $x \in X$  and  $m \in \{1, \dots, M\}$

$$\mathcal{NN}_{\theta^{(m)}}^f(x) := \left(\hat{\mu}^{\theta^{(m)}}(x), \hat{\sigma}_n^{\theta^{(m)}}(x)\right). \quad (42)$$

This then defines the learned predictive distribution for each NN in regression as

$$p_{\theta^{(m)}}(y|x) = \mathcal{N}\left(y; \hat{\mu}^{\theta^{(m)}}(x), (\hat{\sigma}_n^{\theta^{(m)}}(x))^2\right). \quad (43)$$

Finally, the ensemble is treated as uniformly-weighted Gaussian mixture model, i.e.,

$$\frac{1}{M} \sum_{m=1}^M p_{\theta^{(m)}}(y|x), \quad (44)$$

which is further approximated using a single Gaussian by matching the first and second moments. The deep ensemble

<sup>19</sup>Lakshminarayanan et al. (2017) also considered in their paper a third step: *adversarial training*. However, as the authors point out, the effectiveness of adversarial training drops quickly as the number of networks in the ensemble increases. Therefore, we do not consider adversarial training in this paper.

predictions for the mean  $\hat{f}$  and for the combined model uncertainty and data noise  $\hat{\sigma}^2$  are given as

$$\hat{f}(x) := \frac{1}{M} \sum_{m=1}^M \hat{\mu}^{\theta^{(m)}}(x), \quad (45)$$

$$\hat{\sigma}^2(x) := \underbrace{\frac{1}{M} \sum_{m=1}^M \left(\hat{\sigma}_n^{\theta^{(m)}}(x)\right)^2}_{\text{data noise}} + \underbrace{\frac{1}{M} \sum_{m=1}^M \left[\hat{\mu}^{\theta^{(m)}}(x) - \hat{f}(x)\right]^2}_{\text{model uncertainty}}. \quad (46)$$

Setting the data noise to zero  $\sigma_n \equiv 0$  in (46) yields the model uncertainty prediction  $\hat{\sigma}_f^2$  as

$$\hat{\sigma}_f^2(x) := \frac{1}{M} \sum_{m=1}^M \left[\hat{\mu}^{\theta^{(m)}}(x) - \hat{f}(x)\right]^2. \quad (47)$$

which defines deep ensembles' UBS as  $\left(\hat{f}(x) \mp c \hat{\sigma}_f(x)\right)$  with a calibration parameter  $c \in \mathbb{R}_{\geq 0}$ .

**Remark B.1** For known data noise  $\sigma_n$ , no estimation is required and one can use an NN  $\mathcal{NN}_\theta^f$  with only one output  $\hat{\mu}^\theta$ . If additionally the data noise  $\sigma_n$  is assumed to be homoskedastic, one can train  $\mathcal{NN}_\theta^f$  using the mean squared error (MSE) with suitably chosen L2-regularization parameter  $\lambda$ . To obtain predictive bounds instead of credible bounds, one can add  $\sigma_n^2$  to (47) at the end.

## B.2. Regression

### B.2.1. CONFIGURATION DETAILS IN REGRESSION

All NN-based methods are fully connected feed forward NNs with ReLU activation functions, implemented in TENSORFLOW.KERAS and trained for  $2^{10}$  (respectively  $2^{14}$  for the solar irradiance data set) epochs of TENSORFLOW.KERAS' Adam stochastic gradient descent with standard learning rate 0.001 and full batch size of all training points. Moreover, weights and biases are initialized uniformly in the interval  $[-0.05, 0.05]$ .

**NOMU Setup.** For the MC-integration of the integral in the NOMU loss (5), i.e., term (c), we use  $l = 128$  and  $l = 256$  artificial input points (we draw new artificial input points in every gradient descent step) in 1D and 2D, respectively.<sup>20</sup> For numerical stability, we use the parameters  $\theta$  that gave the best training loss during the training which are not necessarily the ones after the last gradient descent step.

**Deep Ensembles Setup.** We consider the proposed number of five ensembles (Lakshminarayanan et al., 2017) with a single output  $\hat{\mu}^\theta$  only (accounting for zero data noise),

<sup>20</sup>In 1D, we tried MC-integration based on uniform samples and MC-integration based on a deterministic grid, where both approaches led to qualitatively similar results and the latter is presented in this paper.

each with three hidden layers consisting of  $2^8$ ,  $2^{10}$  and  $2^9$  nodes (resulting in  $\approx 4$  million parameters). We train them on standard regularized mean squared error (MSE) with regularization parameter  $\lambda = 10^{-8}/n^{\text{train}}$  chosen to represent the same data noise assumptions as NOMU. Analogously, we choose  $\lambda = 10^{-19}/n^{\text{train}}$  as regularization parameter for the solar irradiance data set.

**MC Dropout Setup.** The MC dropout network is set up with three hidden layers as well, with  $2^{10}$ ,  $2^{11}$  and  $2^{10}$  nodes (resulting in  $\approx 4$  million parameters). Both training and prediction of this model is performed with constant dropout probability  $p := p_i = 0.2$ , proposed in (Gal & Ghahramani, 2016). We perform 100 stochastic forward passes. To represent the same data noise assumptions as NOMU and deep ensembles we set the regularization parameter to  $\lambda = (1 - p) \cdot 10^{-8}/n^{\text{train}} = (1 - 0.2) \cdot 10^{-8}/n^{\text{train}}$  (respectively  $\lambda = (1 - 0.2) \cdot 10^{-19}/n^{\text{train}}$  for the solar irradiance data set) (based on equation (7) from (Gal & Ghahramani, 2016)).

**Gaussian Process Setup.** Finally, we compare to a Gaussian process with RBF-kernel,

$$k_\pi(x, x') := \kappa \cdot e^{-\left(\frac{\|x-x'\|_2^2}{h^2}\right)}, \quad (48)$$

with hyperparameters  $\pi := (\kappa, h)$ , where the prior variance parameter is set to  $\kappa := 4$  (cp. to  $\ell_{\max} = 2$  for NOMU), the data noise level is set to  $10^{-7}$ ,<sup>21</sup> and the length scale parameter  $h$  is optimized in the range  $[10^{-5}, 10^5]$  using 10 restarts.<sup>22</sup>

### B.2.2. PERFORMANCE MEASURES

In the following, we give a detailed view on the two performance measures we use to assess the quality of UBS in the 1D and 2D regression settings.

In the following, let

$$(\underline{UB}_c(x), \overline{UB}_c(x)) := \left(\hat{f}(x) \mp c \hat{\sigma}_f(x)\right) \quad (49)$$

denote UBS obtained from any of the considered models via a model prediction  $\hat{f}$ , a model uncertainty prediction  $\hat{\sigma}_f$ , and a calibration parameter  $c \in \mathbb{R}_{\geq 0}$ . Furthermore, we use the following shorthand notation:

$$\mathcal{UB}_c(x) := (\underline{UB}_c(x), \overline{UB}_c(x)). \quad (50)$$

**Mean Width vs. Coverage Probability.** We first formalize the concepts of mean width (MW) and coverage probability (CP). Then we define the measure AUC.

**Definition B.2 (COVERAGE PROBABILITY)** Let  $D^{\text{val}}$  denote a finite set of input-output validation points, and let

<sup>21</sup>This is mainly used for numerical stability.

<sup>22</sup>We use *GaussianProcessRegressor* from SCIKIT-LEARN.

$\mathcal{UB}_c$  denote UBS for a given calibration parameter  $c$ . Then the coverage probability is defined as

$$CP(D^{\text{val}} | \mathcal{UB}_c) := \frac{1}{|D^{\text{val}}|} \sum_{(x, y) \in D^{\text{val}}} \mathbb{1}_{\{\underline{UB}_c(x) \leq y \leq \overline{UB}_c(x)\}}. \quad (51)$$

**Definition B.3 (MEAN WIDTH)** Let  $D^{\text{val}}$  denote a set of input-output validation points, and let  $\mathcal{UB}_c$  denote UBS for a given calibration parameter  $c$ . Then the mean width is defined as

$$MW(D^{\text{val}} | \mathcal{UB}_c) := \frac{1}{|D^{\text{val}}|} \sum_{(x, y) \in D^{\text{val}}} |\overline{UB}(x) - \underline{UB}(x)|. \quad (52)$$

**Remark B.4** Note that in Definition B.3, uncovered points at which UBS (for some fixed calibration parameter  $c$ ) are narrow have a positive effect on overall mean width. In order not to reward such overconfident mispredictions, a possible remedy is to consider in (52) only the subset  $D^{\text{capt}} \subset D^{\text{val}}$  of validation points captured by the UBS at hand, i.e.,

$$D^{\text{capt}} := \{(x, y) \in D^{\text{val}} : \underline{UB}(x) \leq y \leq \overline{UB}(x)\}.$$

However, focusing on captured data points only punishes bounds that capture some points with large widths and almost cover others with small widths unnecessarily harshly compared to bounds for which the reverse is true. In other words, a slight change in calibration parameter  $c$  can lead to very diverse evaluations of UBS that have been assessed almost equal under the original  $c$ . Since ultimately we are interested in comparing UBS based on a range of calibration parameters (see Measure 1 below) we hence decide to include all validation points in the calculation of MW in our experiments.

Ideally, MW should be as small as possible, while CP should be close to its maximal value 1. Clearly, CP is counter-acting MW. This naturally motivates considering ROC-like curves, plotting MW against CP for a range of calibration parameters  $c$ , and comparing different UBS based on their area under the curves (AUC).

**Measure 1 (AUC)** Let  $D^{\text{val}}$  denote a set of input-output validation points. Define further  $c^*$  as the minimal calibration parameter achieving full coverage of  $D^{\text{val}}$  for a given model of UBS, i.e.,

$$c^* := \arg \min_{c \geq 0} \{CP(D^{\text{val}} | \mathcal{UB}_c) = 1\}.$$

AUC is then defined as the integral of the following curve

$$\{(CP(D^{\text{val}} | \mathcal{UB}_c), MW(D^{\text{val}} | \mathcal{UB}_c)) : c \in [0, c^*]\}.^{23}$$

<sup>23</sup>In our experiments, we approximated this integral via the trapezoidal rule.

**Negative Log Predictive Density.** In the following, we first define the *average*<sup>24</sup> negative log Gaussian predictive density (NLPD) and then present our second measure  $NLPD_{\min}$ .

**Definition B.5 (NLPD)** Let  $D^{val}$  denote a set of input-output validation points, and let  $\mathcal{UB}_c$  denote UBs for a given calibration parameter  $c$  with corresponding model prediction  $\hat{f} : X \rightarrow \mathbb{R}$  and model uncertainty prediction  $\hat{\sigma}_f : X \rightarrow \mathbb{R}_{\geq 0}$ . Then NLPD is defined as<sup>25</sup>

$$NLPD(D^{val}|\mathcal{UB}_c) := \quad (53)$$

$$\frac{1}{|D^{val}|} \sum_{(x,y) \in D^{val}} \left[ \frac{(y - \hat{f}(x))^2}{2(c\hat{\sigma}_f(x))^2} + \ln((c\hat{\sigma}_f(x))^2) \right] \quad (54)$$

The first term in NLPD measures the error of the model prediction, where large errors can be attenuated by large uncertainties while the second term penalizes logarithmically larger uncertainties. Thus, NLPD penalizes both over-confident ( $c\hat{\sigma}_f(x) \approx 0$ ) wrong predictions as well as under-confident ( $c\hat{\sigma}_f(x) \gg 0$ ) predictions.

We define the second measure as the minimal value of the NLPD when varying the calibration parameter  $c$ .

**Measure 2 (MINIMUM NLPD)** Let  $D^{val}$  denote a set of input-output validation points, and let  $\mathcal{UB}_c$  denote UBs for a given calibration parameter  $c$ . Then the  $NLPD_{\min}$  is defined as

$$NLPD_{\min} := \min_{c \in \mathbb{R}_{\geq 0}} NLPD(D^{val}|\mathcal{UB}_c). \quad (55)$$

**Remark B.6 (CALIBRATION)** Different approaches of obtaining UBs require rather different scaling to reach similar CP (as well as MW). For instance, as mentioned above, we found that the calibration parameter  $c$  required to achieve a certain value of CP typically is larger for deep ensembles than those of the remaining methods by a factor of approximately 10. Therefore, in practice it is important to find a well-calibrated parameter  $c$ . Standard calibration techniques can be applied to NOMU (e.g. methods based on isotonic regression Kuleshov et al. (2018), or when assuming Gaussian marginals of the posterior one can select  $c$  as the  $\arg \min_{c \in \mathbb{R}_{\geq 0}} NLPD(D^{val}|\mathcal{UB}_c)$  on a validation set  $D^{val}$ .

<sup>24</sup>We remark that NLPD can be interpreted as average marginal predictive density over the validation set  $D^{val}$ , assuming these marginals are Gaussian with mean  $\hat{f}$  and variance  $c\hat{\sigma}_f$ . In particular, we refrain from posing assumptions of posterior independence, that we believe are highly flawed, i.e., NLPD should not be interpreted as joint negative log predictive density.

<sup>25</sup>We ignore constants that are independent of  $\hat{f}$  and  $\hat{\sigma}_f$ .

### B.2.3. DETAILED SYNTHETIC FUNCTIONS RESULTS IN REGRESSION

**Results 1D.** In Table 4 (AUC) and Table 5 ( $NLPD_{\min}$ ), we present detailed results, which correspond to the presented ranks from Table 2 in the main paper.

**Results 2D.** Test functions for 2D input are taken from the same library as in the 1D setting.<sup>26</sup> Specifically, we select the following 11 different test functions: *Sphere*, *G-Function*, *Goldstein-Price*, *Levy*, *Bukin N.6*, *Rosenbrock*, *Beale*, *Camel*, *Perm*, *Branin*, *Styblisnkis-Tang*.

In Table 6, we present median values of AUC and  $NLPD_{\min}$  across all 5500 runs (500 runs for 11 test functions) for each algorithm. We also provide a 95% bootstrap confidence interval (CI) to assess statistical significance. We observe a similar ranking of the different algorithms as in 1D, i.e., NOMU and DE are ranked first in AUC; and the GP is ranked first in  $NLPD_{\min}$  followed by NOMU and DE, who share the second rank.

### B.2.4. DETAILED CHARACTERISTICS OF UNCERTAINTY BOUNDS

**UB Characteristics in 1D.** Within the one-dimensional setting, characteristics of NOMU UBs can be nicely compared to those of the benchmark approaches. Figure 12 exemplarily shows typical outcomes of the UBs on a number of selected test functions as obtained in one run.

- **Deep Ensembles UBS:** Throughout the experiment, we observe that deep ensembles, while sometimes nicely capturing increased uncertainty in regions of high second derivative (e.g. around the kink in Figure 12c; pursuant in some form desiderata D4), still at times leads to UBS of somewhat arbitrary shapes. This can be seen most prominently in Figure 12a around  $x \approx -0.25$ , in Figure 12d around  $x \approx -0.8$  or in Figure 12f around  $x \approx 0.2$ . Moreover, deep ensembles' UBS are very different in width, with no clear justification. This can be seen in fig. 12a when comparing the UBS for  $x \geq 0$  against the UBS for  $x \leq 0$  and at the edges of the input range in Figures 12d and 12e. In addition, we frequently observe that deep ensembles UBS do not get narrow at training points, as for instance depicted in Figure 12b for  $x < -0.5$ , in Figure 12d for  $x > 0.2$ , or in Figure 12f for  $x \in [-1, -0.7]$  and therefore are not able to handle well small or zero data noise.

- **MC Dropout UBS:** MC dropout consistently yields tube-like UBS that in particular do not narrow at training points. Interestingly, we remark that throughout the experiment MC dropout samples frequently exhibit stepfunction-like shapes (see e.g. Figure 12f at  $x \approx 0.5$  or Figure 12a

<sup>26</sup>[www.sfu.ca/~surjano/optimization.html](http://www.sfu.ca/~surjano/optimization.html) All test functions are scaled to  $X = [-1, 1]^2$  and  $f(X) = [-1, 1]$ .

FUNCTION	NOMU		GP		MCDO		DE	
	AUC	95%-CI	AUC	95%-CI	AUC	95%-CI	AUC	95%-CI
ABS	<b>0.074</b>	[0.066, 0.079]	0.179	[0.157, 0.213]	0.157	[0.15 , 0.166]	<b>0.076</b>	[0.068, 0.087]
STEP	0.287	[0.258, 0.305]	1.472	[1.288, 1.646]	0.253	[0.237, 0.268]	<b>0.138</b>	[0.128, 0.151]
KINK	<b>0.083</b>	[0.076, 0.089]	0.228	[0.202, 0.269]	0.217	[0.208, 0.226]	<b>0.087</b>	[0.073, 0.099]
SQUARE	0.117	[0.111, 0.126]	<b>0.006</b>	[0.005, 0.007]	0.382	[0.356, 0.406]	0.135	[0.124, 0.15 ]
CUBIC	0.07	[0.065, 0.075]	<b>0.006</b>	[0.005, 0.006]	0.101	[0.095, 0.105]	0.1	[0.092, 0.106]
SINE 1	1.103	[1.033, 1.164]	1.325	[1.294, 1.345]	<b>0.902</b>	[0.872, 0.931]	1.206	[1.155, 1.262]
SINE 2	0.385	[0.373, 0.401]	0.857	[0.835, 0.886]	<b>0.356</b>	[0.35 , 0.361]	0.5	[0.466, 0.525]
SINE 3	<b>0.203</b>	[0.193, 0.214]	0.481	[0.423, 0.571]	0.276	[0.264, 0.289]	<b>0.199</b>	[0.188, 0.212]
FORRESTER	0.189	[0.18 , 0.2 ]	<b>0.099</b>	[0.089, 0.112]	0.258	[0.243, 0.276]	0.252	[0.238, 0.269]
LEVY	<b>0.403</b>	[0.388, 0.423]	1.266	[1.141, 1.342]	<b>0.375</b>	[0.362, 0.388]	0.45	[0.427, 0.476]

Table 4. Detailed results of the AUC performance measure for NOMU, GP, MCDO and DE, for all ten 1D synthetic functions. Shown are the medians and a 95% bootstrap confidence interval over 500 runs. Winners are marked in green.

FUNCTION	NOMU		GP		MCDO		DE	
	NLPD <sub>MIN</sub>	95%-CI						
ABS	<b>-2.854</b>	[-2.946, -2.8 ]	-2.589	[-2.69 , -2.519]	-1.757	[-1.802, -1.692]	<b>-2.911</b>	[-3.015, -2.763]
STEP	-1.045	[-1.116, -0.974]	-0.37	[-0.527, -0.17 ]	-0.782	[-0.845, -0.686]	<b>-2.49</b>	[-2.585, -2.361]
KINK	<b>-2.737</b>	[-2.804, -2.694]	-2.42	[-2.502, -2.31 ]	-1.275	[-1.327, -1.217]	<b>-2.805</b>	[-2.931, -2.677]
SQUARE	-2.448	[-2.508, -2.411]	<b>-5.345</b>	[-5.434, -5.266]	-0.559	[-0.649, -0.517]	-2.266	[-2.368, -2.164]
CUBIC	-2.979	[-3.037, -2.943]	<b>-5.601</b>	[-5.632, -5.563]	-2.41	[-2.466, -2.334]	-2.645	[-2.704, -2.592]
SINE 1	<b>0.102</b>	[ 0.039, 0.184]	<b>-0.002</b>	[-0.079, 0.099]	<b>0.095</b>	[ 0.069, 0.128]	<b>0.092</b>	[ 0.043, 0.164]
SINE 2	<b>-1.346</b>	[-1.377, -1.318]	-1.013	[-1.067, -0.951]	-1.032	[-1.058, -1.004]	-0.921	[-0.96 , -0.879]
SINE 3	<b>-1.553</b>	[-1.612, -1.47 ]	<b>-1.59</b>	[-1.83 , -1.35 ]	-1.074	[-1.118, -1.01 ]	<b>-1.665</b>	[-1.754, -1.576]
FORRESTER	-1.975	[-2.034, -1.91 ]	<b>-3.733</b>	[-3.823, -3.647]	-1.1	[-1.191, -1.029]	-1.753	[-1.792, -1.685]
LEVY	<b>-1.115</b>	[-1.143, -1.067]	-0.403	[-0.441, -0.371]	-0.765	[-0.787, -0.729]	<b>-1.037</b>	[-1.078, -0.973]

Table 5. Detailed results of the NLPD<sub>MIN</sub> performance measure for NOMU, GP, MCDO and DE, for all ten 1D synthetic functions. Shown are the medians and a 95% bootstrap confidence interval over 500 runs. Winners are marked in green.

MODEL	AUC	NLPD <sub>MIN</sub>
NOMU	<b>0.42 [0.41, 0.42]</b>	-0.99 [-1.01, -0.96]
GP	0.43 [0.42, 0.44]	<b>-1.22 [-1.25, -1.19]</b>
MCDO	0.45 [0.44, 0.45]	-0.61 [-0.62, -0.60]
DE	<b>0.42 [0.41, 0.43]</b>	-0.95 [-0.97, -0.93]

Table 6. Aggregate results for NOMU, GP, MCDO and DE for the set of all eleven 2D synthetic functions. Shown are the medians and a 95% bootstrap confidence interval of each measure across all runs. Winners are marked in green.

for  $x \in [-0.5, 0]$ ). This effect intensifies with increasing training time.

- **NOMU UBs:** In contrast, NOMU displays the behaviour it is designed to show. Its UBs nicely tighten at training points and expand in between and thus NOMU fulfills **D1–D3** across all considered synthetic test functions.
- **Gaussian Process UBs:** The quality of the RBF-Gaussian process’ UBs (as judged in this simulated setting) naturally varies with the true underlying function. While the UBs nicely capture parts of the true function with low widths in Figures 12b and 12f they have a hard time accurately enclosing true functions that are not as conformant with the prior belief induced by the choice of the RBF kernel (e.g. Figures 12a and 12c). Nonetheless, we also observe instances in which the training points

are misleading to the GP’s mean predictions even when considering ground truth functions for which this choice of kernel is very suitable. This manifests in over-confident mean predictions far away from the data generating true function (Figure 12e) or over-swinging behavior of the fitted mean (Figure 12d). Indeed, it is true that one could find better function-specific kernels. However, the RBF kernel is a good generic choice when evaluated across many different test functions without any specific prior information, which is why we choose this kernel for our comparison.

**UB Characteristics in 2D.** In Figure 14 (NOMU) and Figure 15 (benchmarks), we visualize the estimated model uncertainty as obtained in one run for the *Styblinski* test function (Figure 13)

• **NOMU (Figure 14):** Analogously as in 1D, we observe that NOMU’s UBs nicely tighten at input training points and expand in-between, with overall steady shapes. Specifically, NOMU’s UBs are larger for extrapolation, e.g.,  $[0, 1] \times [0.5, 1]$ , compared to regions which are *surrounded* by input training data points, e.g.,  $[-0.25, 0.25] \times [-0.25, -0.75]$ , even though the distance to the closest input training point is approximately the same. Thus, NOMU’s UBs do not only depend on the

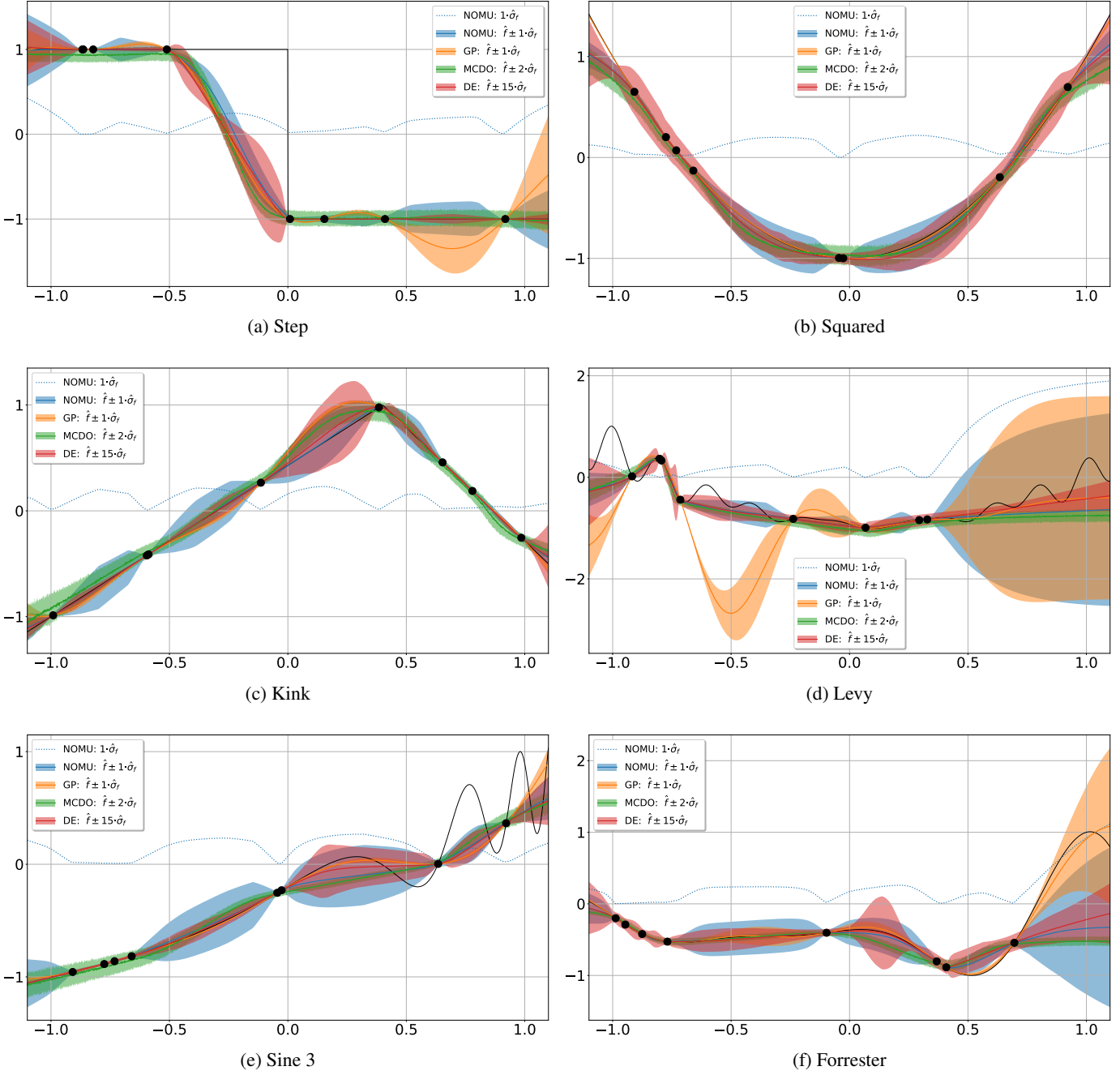


Figure 12. Visualisations of resulting UBs for NOMU, GP, MCDO and DE for a selection of test functions.

distance to the closest training point but rather on the arrangement of all the surrounding training points.

- **Benchmarks (Figure 15):** Similarly as in 1D, we observe that the RBF-based Gaussian process's UBs do have the expected smooth and isotropic shape with zero model uncertainty at the input training points. Moreover, as in

1D, MC dropout's UBs exhibit a tubular shape of equal size ( $\approx 0$ – $0.25$ ) across the whole input space. Whilst deep ensembles nicely captures zero model uncertainty at input training points, it again exhibits the somehow arbitrary behaviour in areas with few input training points (cp. 1D).

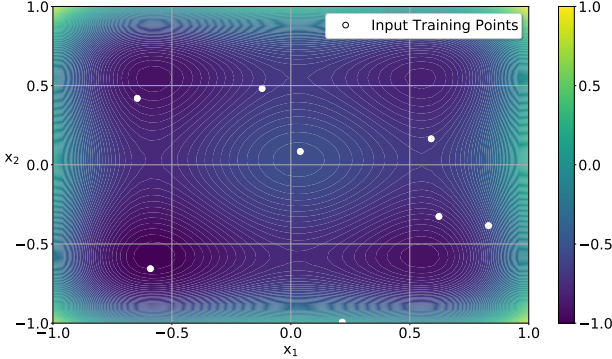


Figure 13. Contour plot of the 2D Styblinski test function.

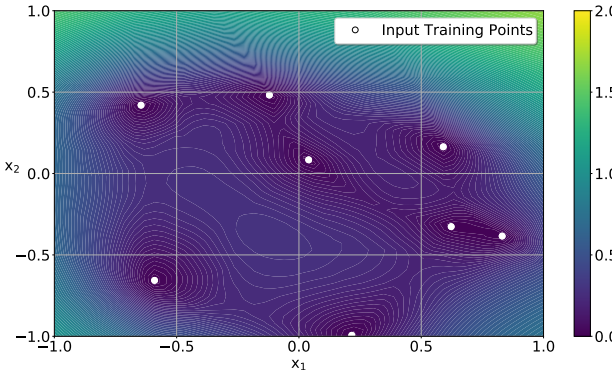


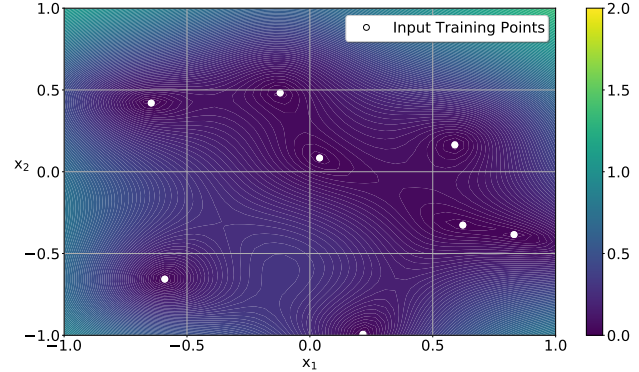
Figure 14. Estimated model uncertainty  $\hat{\sigma}_f$  of NOMU for a single run of the Styblinski test function.

#### B.2.5. DETAILED REAL-DATA TIME SERIES RESULTS

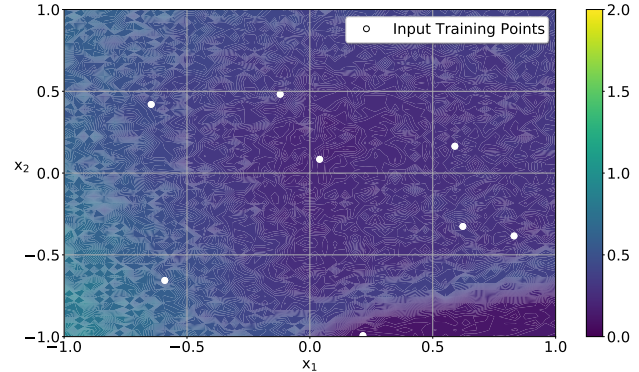
Figure 16 visualizes the UBs from NOMU and the benchmark algorithms. As becomes evident, NOMU manages to best fit the training data<sup>27</sup>, while keeping model uncertainty in-between training points. The corresponding performance measures for this specific run are given in Table 7.

MODEL	AUC	NLPD <sub>MIN</sub>
NOMU	0.34	-1.48
GPR	0.80	-1.03
MCDO	0.25	-1.43
DE	0.28	-1.46

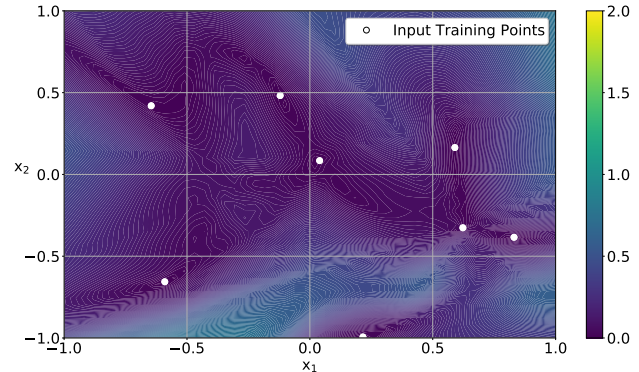
Table 7. Performance measures for solar irradiance time series.



(a) GP with calibration constant  $c = 1$ .



(b) MCDO with calibration constant  $c = 10$ .



(c) DE with calibration constant  $c = 15$ .

Figure 15. Estimated model uncertainty of Gaussian process (GP), MC dropout (MCDO) and deep ensembles (DE) for a single run of the Styblinski test function.

<sup>27</sup>(Gal & Ghahramani, 2016) consider the same data set to compare UBs of MC dropout and GPs. In this work however, NNs are trained for  $10^6$  epochs possibly explaining why MC dropout more nicely fits the training data in their case.

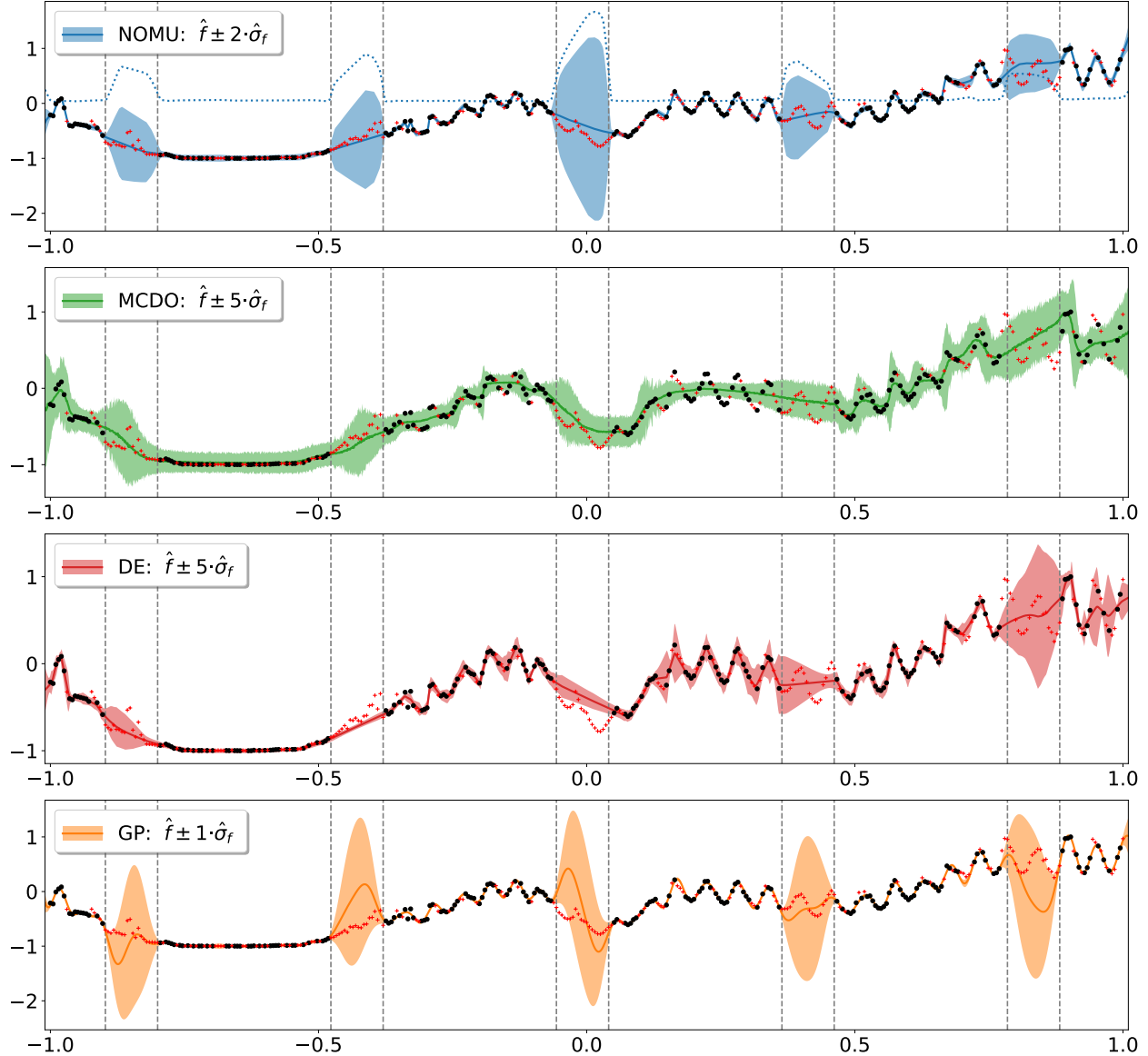


Figure 16. Visualization of each algorithm’s model prediction (solid lines) and UBs (shaded areas) on the solar irradiance data set. Training and validation points are shown as black dots and red crosses, respectively. We present UBs obtained by NOMU ( $c=2$ ) compared to the benchmarks MC dropout (MCDO) ( $c=5$ ), deep ensembles (DE) ( $c=5$ ) and Gaussian process (GP) ( $c=1$ ). Additionally, NOMU’s estimated and scaled model uncertainty  $2\hat{\sigma}_f$  is shown as a dotted line.

### B.3. Bayesian Optimization

#### B.3.1. CONFIGURATION DETAILS IN BAYESIAN OPTIMIZATION

In the following, we describe the detailed hyperparameter setup of all algorithms.

**NOMU Setup.** For NOMU, we set  $\pi_{\text{sqr}} = 1$  and  $\ell_{\min} = 1e-6$  and otherwise use the exact same hyperparameters as in 1D and 2D regression (see in Section 5.1 the paragraph **NOMU Setup**).

**Deep Ensembles Setup.** For deep ensembles, we use the exact same hyperparameters as in 1D and 2D regression (see Appendix B.2.1).

**MC Dropout Setup.** For MC dropout, due to computational constraints, we were only able to use 10 stochastic forward passes (instead of 100 in the regression setting). However, this still results in an increase in compute time by a factor 10 of every single acquisition function evaluation compared to NOMU. Otherwise, we use the exact same hyperparameters as in 1D and 2D regression (see Appendix B.2.1).

**Gaussian Process Setup.** For Gaussian processes, we now also optimize the prior variance parameters  $\kappa$  (in the case of pGP), which is initialized  $\kappa := 1$  and optimized in the default range  $[1e-5, 1e5]$ . Otherwise, we use the exact same hyperparameters as in 1D and 2D regression (see Appendix B.2.1).

#### B.3.2. CALIBRATION IN BAYESIAN OPTIMIZATION

**MW SCALING.** In general, having a good understanding of the prior scale is very hard. Nevertheless, often it is easier to have at least some intuition in which order of magnitude the posterior UBs should be on average. When function values approximately range in  $[-1, 1]$ , it is reasonable to require that after observing 8 initial points the mean width (MW) of the UBs lies within the order of magnitudes 0.05 and 0.5. Hence our motivation for choosing the calibration parameter  $c$  accordingly. An advantage of such a calibration is that it can be applied to every method equally, whereas there is in general no clear notion of setting the prior scale of two different methods (e.g. MC dropout and deep ensembles) to the same value. Note, that we only use MW to calibrate  $c$  directly after mean and variance predictions were fit based on the 8 initial data points. So MW is not fixed when further data points are observed in subsequent steps of the BO.

**DYNAMIC C.** The initial choice of  $c$  can still be corrected in each BO step. Certainly, in the noiseless case it does not make sense to pick an input point  $x_{i'}$  that is identical to an already observed input point  $x_i, i < i'$ , where nothing new is to be learned. Therefore, we want our NN-agent to get “bored” if its acquisition function optimization would

suggest to pick an input point  $x_{i'} \approx x_i, i < i'$ . The idea of DYNAMIC C is to encourage the agent, in case it was “bored”, to become more “curious” to explore something new instead of picking a “boring” input point. This can be achieved by iteratively increasing  $c$  until the acquisition function optimization suggests an input point  $x_{i'} \not\approx x_i, \forall i < i'$ . We then only apply the expensive function evaluation for  $x_{i'} \not\approx x_i, \forall i < i'$  that we obtained after increasing  $c$  enough to not “bore” the NN. However, towards the last BO-steps, if we already know approximately where a global optimum is and we only want to fix the last digits of the optimizer, we have to evaluate the function closer to already observed points. In contrast, a very “young” NN (i.e., a network that has been trained on few training points) should get “bored” much more easily, since it is not sensible to exploit a given local optimum up to the last digits, when there is plenty of time to reach other, possibly better local optima.

Thus, it makes sense to first explore on a large scale where the good local optima are approximately, then to find out which of them are the best ones and finally to exploit the best one in greater detail at the very end.

Therefore, we want the threshold  $\delta_i$ , that determines if  $x_{i'} \stackrel{\delta_{i'}}{\approx} x_i \iff \|x_{i'} - x_i\|_2 \leq \delta_{i'}$  to decrease in each BO step. In our experiment, we choose an exponential decay of

$$\delta_i = \delta_{n^{\text{start}}} \cdot \left( \frac{\delta_{n^{\text{end}}}}{\delta_{n^{\text{start}}}} \right)^{(i-n^{\text{start}})/(n^{\text{end}}-n^{\text{start}})}, \quad (56)$$

with  $\delta_{n^{\text{start}}} = \frac{1}{16}$  and  $\delta_{n^{\text{end}}} = 0.01$ .

Concretely, we only evaluate  $f$  at  $x_{i'}$  if  $\|x_{i'} - x_i\|_2 > \delta_{i'} \forall i < i'$  is fulfilled. Otherwise we double  $c$  until it is fulfilled (With larger  $c$  more emphasis is put on exploration, so there is a tendency that  $x_{i'}$  will be further away from the observed input points the larger we pick  $c$ , if D3 (Out-of-Sample) is fulfilled). After doubling  $c$  15 times without success, we evaluate  $f$  at  $x_{i'}$  no matter how close it is to the already observed input points (for methods that have severe troubles to fulfill D3 (Out-of-Sample), such as MCDO, even doubling  $c$  infinite times would not help if the maximal uncertainty is within an  $\delta_{i'}$ -ball around an already observed input point).

#### B.3.3. DETAILED RESULTS IN BAYESIAN OPTIMIZATION

In Table 8, we present the mean final regrets, which correspond to the ranks shown in Table 3 in the main paper.

#### B.3.4. REGRET PLOTS

In Figures 17–19, we present the regret plots for each test function and both MW values.

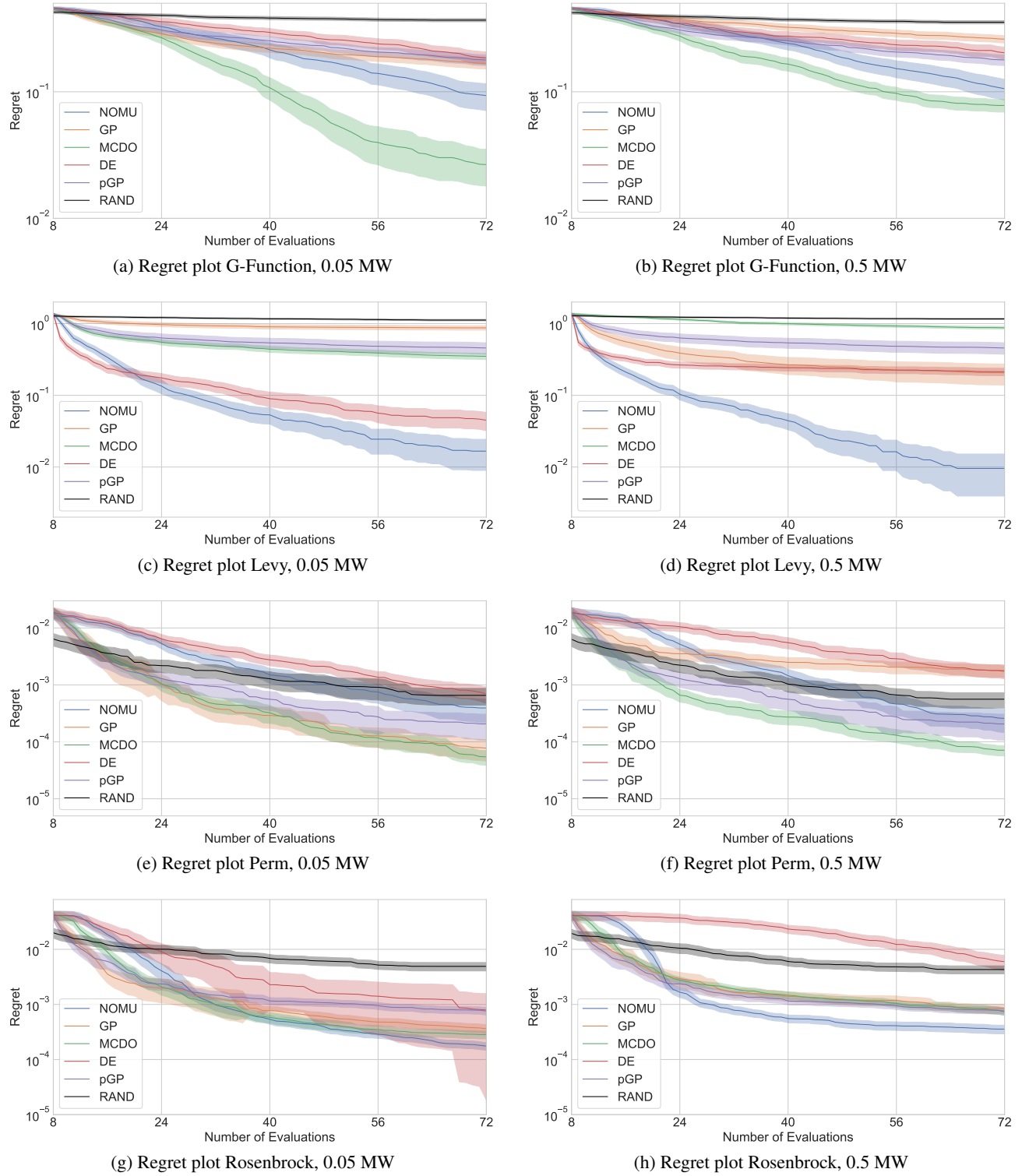


Figure 17. Regret plots for all 5D test functions and MWs of 0.05 and 0.5, respectively. We show regrets averaged over 100 runs (solid lines) with 95% CIs.

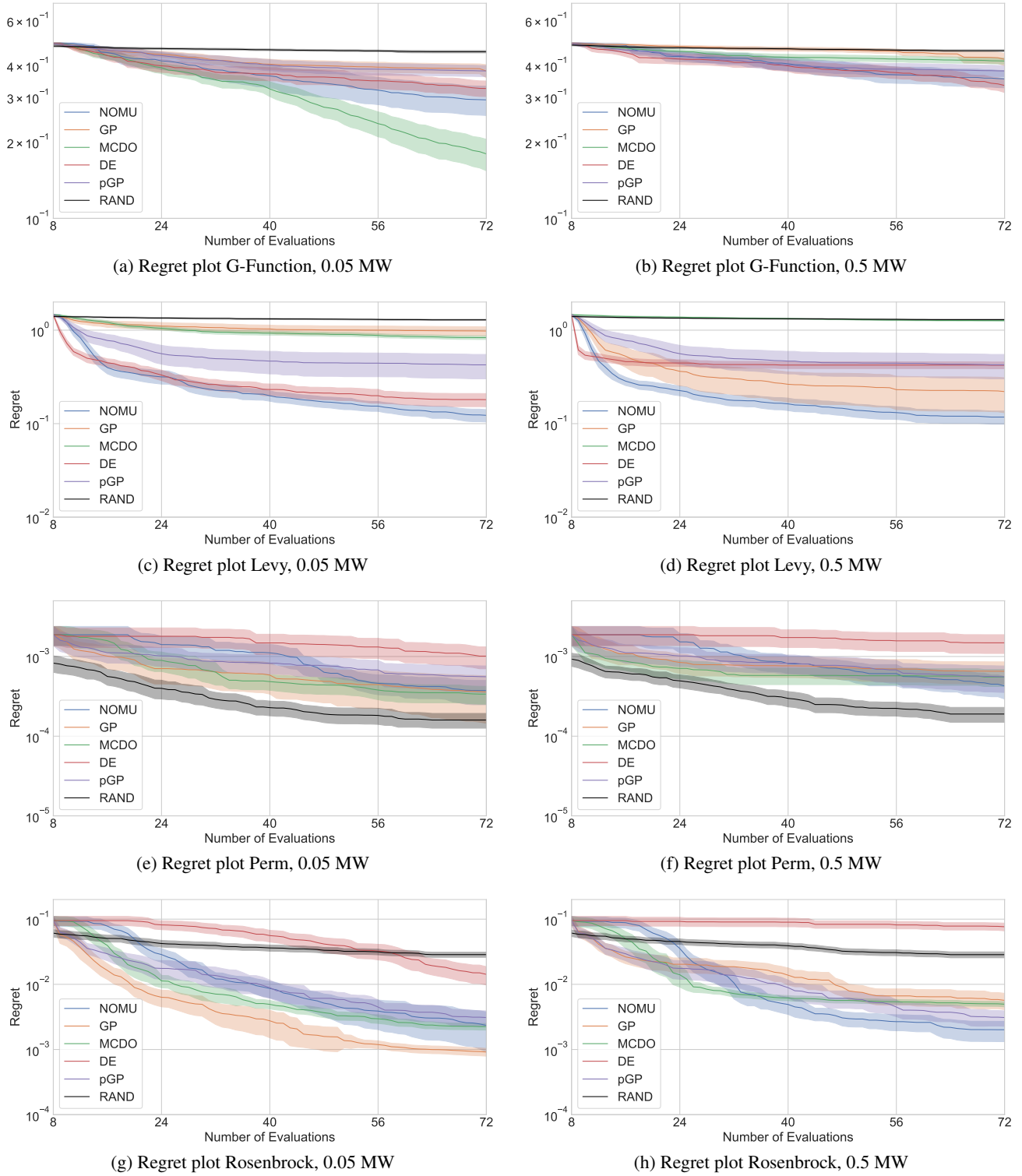


Figure 18. Regret plots for all 10D test functions and MWs of 0.05 and 0.5, respectively. We show regrets averaged over 100 runs (solid lines) with 95% CIs.

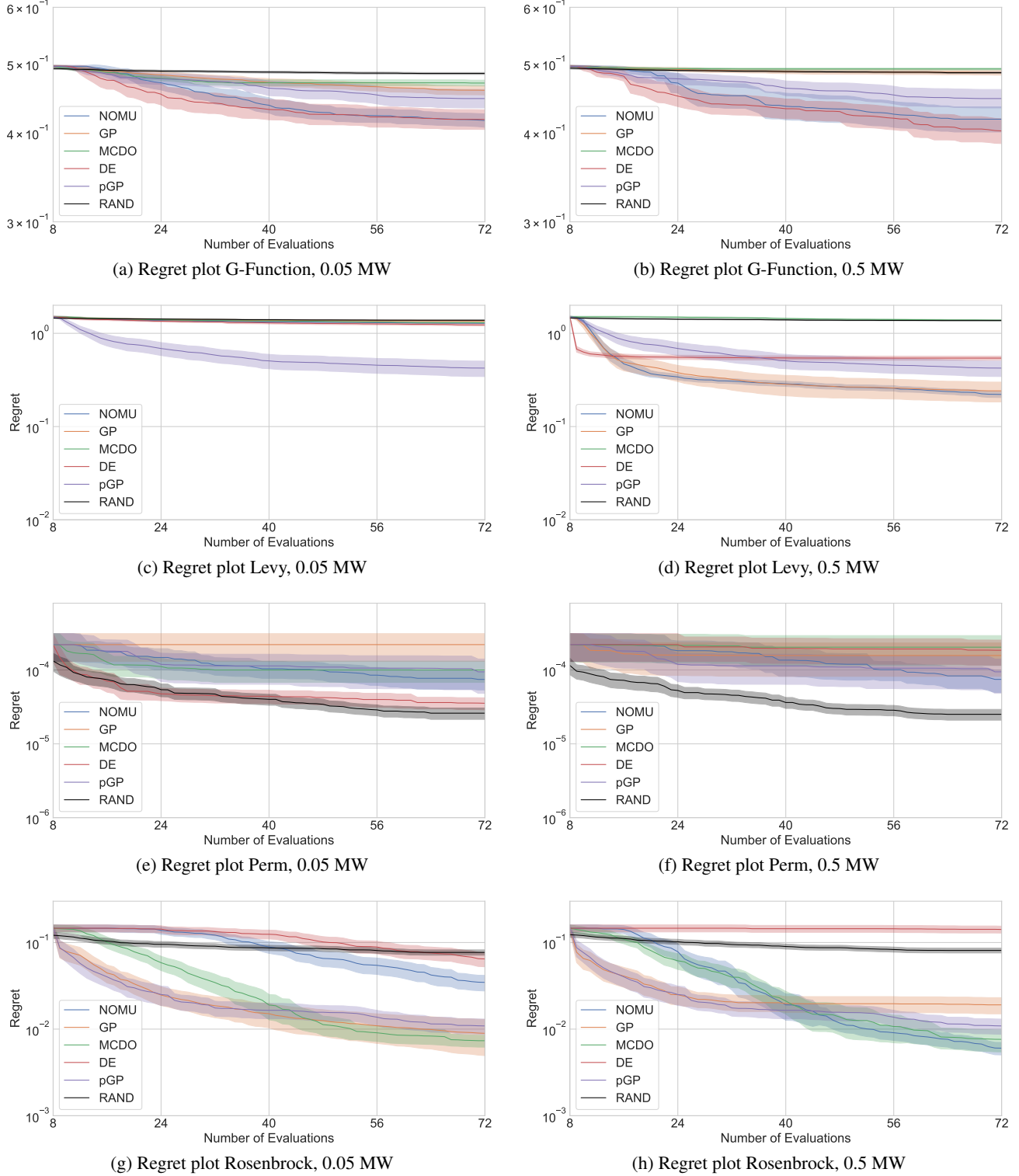


Figure 19. Regret plots for all 20D test functions and MWs of 0.05 and 0.5, respectively. We show regrets averaged over 100 runs (solid lines) with 95% CIs.

FUNCTIONS	NOMU		GP		MCDO		DE		PGP	RAND
	MW 0.05	MW 0.5								
G-FUNCTION5D	9.33e-2±2.23e-2	1.06e-1±1.97e-2	1.68e-1±1.62e-2	2.60e-1±1.72e-2	2.66e-2±8.57e-3	7.80e-2±8.82e-3	1.86e-1±2.07e-2	2.03e-1±2.20e-2	1.78e-1±1.73e-2	3.63e-1±1.34e-3
LEVY5D	1.67e-2±7.68e-3	9.56e-3±5.63e-3	8.72e-1±6.12e-2	2.06e-1±6.72e-2	3.51e-1±3.52e-2	8.75e-1±3.74e-2	4.49e-2±1.28e-2	2.13e-1±2.55e-2	4.57e-1±8.34e-2	1.16 ±2.72e-3
PERM5D	3.93e-4±1.75e-4	2.58e-4±1.13e-4	7.76e-5±3.19e-5	1.80e-3±4.44e-4	5.50e-5±1.58e-5	7.11e-5±1.45e-5	6.96e-4±2.20e-4	1.73e-3±4.55e-4	2.06e-4±9.96e-5	6.55e-4±2.63e-5
ROSENROCK5D	1.75e-4±2.76e-5	3.57e-4±6.39e-5	3.62e-4±6.52e-5	8.44e-4±1.62e-4	2.83e-4±4.64e-5	7.35e-4±1.08e-4	7.93e-4±7.74e-4	5.96e-3±1.78e-3	7.56e-4±1.15e-4	4.58e-3±9.69e-5
<i>Average Regret 5D</i>										
	2.76e-2±5.89e-3	2.90e-2±5.11e-3	2.60e-1±1.58e-2	1.17e-1±1.73e-2	9.44e-2±9.06e-3	2.39e-1±9.60e-3	5.8 e-2±0.09e-3	1.06e-1±8.44e-3	1.59e-1±2.13e-2	3.83e-1±7.59e-4
G-FUNCTION10D	2.92e-1±3.85e-2	3.53e-1±2.74e-2	3.79e-1±2.24e-2	4.21e-1±2.35e-2	1.79e-1±2.54e-2	4.15e-1±1.12e-2	3.24e-1±2.28e-2	3.33e-1±2.06e-2	3.80e-1±1.90e-2	4.56e-1±7.40e-4
LEVY10D	1.23e-1±1.85e-2	1.18e-1±1.89e-2	9.78e-1±1.08e-1	2.20e-1±8.96e-2	8.34e-1±3.85e-2	1.27	1.65e-2	1.81e-1±2.90e-2	4.22e-1±3.50e-2	4.26e-1±1.24e-1
PERM10D	3.74e-4±1.26e-4	4.27e-4±1.34e-4	3.59e-4±2.13e-4	6.52e-4±2.04e-4	3.37e-4±8.49e-5	5.53e-4±1.33e-4	1.01e-3±3.10e-4	1.48e-3±3.92e-4	5.57e-4±2.03e-4	1.60e-4±4.44e-6
ROSENROCK10D	2.34e-3±1.43e-3	2.01e-3±6.91e-4	9.14e-4±1.25e-4	5.67e-3±1.60e-3	2.25e-3±2.58e-4	4.96e-3±4.40e-4	1.42e-2±4.43e-4	7.65e-2±1.03e-2	3.09e-3±8.20e-4	2.95e-2±4.76e-4
<i>Average Regret 10D</i>										
	1.04e-1±1.07e-2	1.18e-1±8.33e-3	3.40e-1±2.76e-2	1.62e-1±2.31e-2	2.54e-1±1.15e-2	4.21e-1±5.00e-3	1.30e-1±9.27e-3	2.08e-1±1.05e-2	2.02e-1±3.15e-2	4.48e-1±5.68e-4
G-FUNCTION20D	4.16e-1±8.99e-3	4.18e-1±1.70e-2	4.59e-1±6.77e-3	4.86e-1±3.95e-3	4.70e-1±4.43e-3	4.92e-1±1.58e-3	4.18e-1±1.33e-2	4.02e-1±1.61e-2	4.47e-1±1.33e-2	4.84e-1±2.86e-4
LEVY20D	1.28 ±0.76e-3	2.21e-1±1.64e-2	1.35 ±2.94e-2	2.42e-1±5.80e-2	1.30 ±2.13e-2	1.38 ±1.54e-2	1.23 ±3.24e-2	5.42e-1±2.72e-2	4.24e-1±7.99e-2	1.37 ±1.78e-3
PERM20D	7.45e-5±2.09e-5	7.46e-5±2.50e-5	2.20e-4±8.98e-5	1.57e-4±7.50e-5	9.98e-5±3.19e-5	2.03e-5±4.88e-5	3.54e-5±6.52e-6	1.85e-4±6.90e-5	9.44e-5±4.61e-5	2.18e-5±6.49e-7
ROSENROCK20D	3.47e-2±7.08e-3	6.03e-3±9.93e-4	8.94e-3±4.00e-3	1.91e-2±4.04e-3	7.35e-3±1.15e-3	7.61e-3±2.15e-3	6.46e-2±1.22e-2	1.41e-1±1.29e-2	1.09e-2±2.17e-3	7.80e-2±9.22e-4
<i>Average Regret 20D</i>										
	4.34e-1±3.76e-3	1.61e-1±5.91e-3	4.55e-1±7.61e-3	1.87e-1±1.46e-2	4.44e-1±5.44e-3	4.71e-1±3.91e-3	4.29e-1±9.25e-3	2.27e-1±8.54e-3	2.20e-1±2.03e-2	4.83e-1±5.07e-4

Table 8. Results for 12 different BO tasks. Shown are the average final regrets per dimension and for each individual function over 100 (5D) and 50 (10D and 20D) runs for an initial mean width (MW) of 0.05 and 0.5, respectively. Winners are marked in green.

## C. Extensions

### C.1. Incorporating Data Noise

We briefly present one straightforward way to incorporate data noise in NOMU.

If  $\sigma_n$  is unknown, one option to learn it, is to add another output  $\hat{\sigma}_n$  to the NOMU architecture and change the loss function to

$$L^\pi(\mathcal{NN}_\theta) := \sum_{i=1}^{n^{\text{train}}} \left( \frac{(\hat{f}(x_i^{\text{train}}) - y_i^{\text{train}})^2}{2(\hat{\sigma}_n(x_i^{\text{train}}))^2} + \ln(\hat{\sigma}_n(x_i^{\text{train}})) \right) + \pi_{\text{sqr}} \cdot \sum_{i=1}^{n^{\text{train}}} \frac{(\hat{r}_f(x_i^{\text{train}}))^2}{2(\hat{\sigma}_n(x_i^{\text{train}}))^2} + \pi_{\text{exp}} \cdot \frac{1}{\lambda_d(X)} \int_X e^{-c_{\text{exp}} \cdot \hat{r}_f(x)} dx, \quad (57)$$

in the case of Gaussian data noise uncertainty. In this case we recommend to first train the model prediction  $\hat{f}$  and the data noise  $\hat{\sigma}_n$  only and then freeze their parameters and train the  $\hat{r}_f$ -network for capturing model uncertainty  $\hat{\sigma}_f$ . Note that in the NOMU loss (5) we implicitly assumed a constant very small and negligible data noise  $\sigma_n^2$ , absorbed as a factor into the hyperparameter  $\pi_{\text{exp}}$  and the regularization factor  $\lambda$ . Therefore, if one wishes to be consistent in these prior assumptions, the hyperparameters  $\pi_{\text{exp}}$  and  $\lambda$  need to be divided by  $2\sigma_n^2$  in eq. (57). Thus, when using the loss (57) instead of the NOMU loss (5),  $\pi_{\text{exp}}$  and  $\lambda$  need to be chosen significantly larger.

In the case of known (heteroscedastic) data noise  $\sigma_n(x)$ , (57) can be simplified, replacing  $\hat{\sigma}_n$  by  $\sigma_n$  and dropping the term  $\ln(\sigma_n)$  (in this case, one can then also drop the  $\hat{\sigma}_n$ -output of the NOMU architecture).

*Predictive* UBs are then obtained as

$$(\hat{f}(x) \mp \sqrt{c_1 \hat{\sigma}_f^2(x) + c_2 \hat{\sigma}_n^2(x)}) \quad (58)$$

with suitable calibration parameters  $c_1, c_2 \in \mathbb{R}_{\geq 0}$ .

In the case of known normally distributed data noise (and under the assumption that the posterior of each  $f(x)$  is Gaussian), it is sufficient to calibrate one calibration parameter  $\tilde{c}$  to obtain approximate  $\alpha$  predictive bounds

$$\left( \hat{f}(x) \mp \Phi^{-1}(1 - \frac{1 - \alpha}{2}) \sqrt{\tilde{c} \hat{\sigma}_f^2(x) + \sigma_n^2(x)} \right), \quad (59)$$

where  $\tilde{c}$  relates to the typically unknown prior scale.

### C.2. NOMU for Upwards and Downwards Directed Hypothesis Classes

As mentioned in Section 4 and discussed in more detail in Appendix A.3, often the set  $\mathcal{H}_{D^{\text{train}}}$  is not upwards directed for typical NN-architectures and eq. (8) of Theorem 4.1 is not fulfilled in general. Therefore, we carefully designed our NOMU algorithm to be able to cope with settings where the set  $\mathcal{H}_{D^{\text{train}}}$  is not upwards and/or downwards directed. The downwards directed property is defined analogously as follows:

**Assumption 2 (DOWNWARDS DIRECTED)** *For every  $f_1, f_2 \in \mathcal{H}_{D^{\text{train}}}$  there exists an  $f \in \mathcal{H}_{D^{\text{train}}}$  such that  $f(x) \leq \min(f_1(x), f_2(x))$  for all  $x \in X$ .*

However, in the following, we discuss a modification of NOMU, which is specifically designed for the case if  $\mathcal{H}_{D^{\text{train}}}$  is indeed upwards and/or downwards directed. In this case, by Theorem 4.1, we can directly solve

$$\arg \max_{h \in \mathcal{H}_{D^{\text{train}}}} \int_X u(h(x) - \hat{f}(x)) dx \quad (60)$$

to obtain an upper UB and/or

$$\arg \min_{h \in \mathcal{H}_{D^{\text{train}}}} \int_X u(h(x) - \hat{f}(x)) dx \quad (61)$$

to obtain a lower UB, without the need for any modifications as used in the proposed NOMU algorithm (we do not need the dashed connections in the architecture from Figure 2, we do not need a specific choice of  $u$  and we do not need to introduce  $\hat{r}_f$  and the final activation function  $\varphi$ ). The UBs obtained in this way *exactly* coincide then with the pointwise upper and lower UBs defined in (7) and (6), respectively.

Moreover in this case,  $\hat{f}$  can be even removed from eqs. (60) and (61) (as can be seen from the proof of Theorem A.2). Thus, in the following loss formulation, we will remove  $\hat{f}$  in the respective term  $(\tilde{c})$ .

### C.2.1. THE ARCHITECTURE

Under Assumption 1 (upwards directed) and Assumption 2 (downwards directed), we therefore propose an architecture consisting of three sub-networks  $\widetilde{\mathcal{NN}}_\theta$  with three outputs: the model prediction  $\hat{f}$ , the estimated lower UB  $\widehat{UB}$  and the estimated upper UB  $\widehat{UB}$  (depicted in Figure 20).

### C.2.2. THE LOSS FUNCTION

From eqs. (60) and (61) we can then directly formulate the following modified NOMU loss function  $\tilde{L}^\pi$ .

**Definition C.1** (NOMU LOSS UPWARDS AND DOWNTWARDS DIRECTED) *Let  $\pi := (\pi_{sqr}, \pi_{exp}, c_{exp}) \in \mathbb{R}_{\geq 0}^3$  denote a tuple of hyperparameters. Let  $\lambda_d$  denote the  $d$ -dimensional Lebesgue measure. Furthermore, let  $u : Y \rightarrow \mathbb{R}$  be strictly-increasing and continuous. Given a training set  $D^{\text{train}}$ , the loss function  $\tilde{L}^\pi$  is defined as*

$$\tilde{L}^\pi(\widetilde{\mathcal{NN}}_\theta) := \underbrace{\sum_{i=1}^{n^{\text{train}}} (\hat{f}(x_i^{\text{train}}) - y_i^{\text{train}})^2}_{(\tilde{a})} \quad (62)$$

$$+ \underbrace{\pi_{sqr} \cdot \sum_{i=1}^{n^{\text{train}}} (\widehat{UB}(x_i^{\text{train}}) - y_i^{\text{train}})^2 + (\widehat{UB}(x_i^{\text{train}}) - \widehat{LB}(x_i^{\text{train}}))^2}_{(\tilde{b})} \quad (63)$$

$$- \underbrace{\pi_{exp} \cdot \frac{1}{\lambda_d(X)} \int_X u(-\widehat{UB}(x)) + u(\widehat{UB}(x)) dx}_{(\tilde{c})}. \quad (64)$$

The interpretations of the three terms  $(\tilde{a})$ ,  $(\tilde{b})$  and  $(\tilde{c})$  are analogous to the ones in the original NOMU loss formulation.

Note that, the three sub-networks: the  $\widehat{UB}$ -network, the  $\widehat{LB}$ -network and the  $\hat{f}$ -network can be also trained independently using the corresponding terms in the loss function. Furthermore, if one is only interested in the upper (lower) UB or  $\mathcal{H}_{D^{\text{train}}}$  is only upwards (downwards) directed, i.e., fulfills either Assumption 1 or Assumption 2, then one can remove the respective sub-network from the architecture as well as the corresponding terms in the loss function.

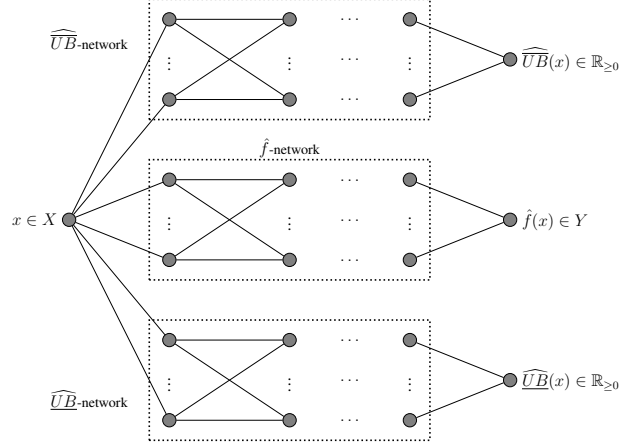


Figure 20. Modification of NOMU's network architecture for upwards and downwards directed hypothesis classes.

Furthermore, note that now the obtained UBs can be asymmetric too.

## References

Amodei, D., Olah, C., Steinhardt, J., Christiano, P. F., Schulman, J., and Mané, D. Concrete problems in AI safety. *Corr*, abs/1606.06565, 2016. URL <http://arxiv.org/abs/1606.06565>.

Baptista, R. and Poloczek, M. Bayesian optimization of combinatorial structures. In *International Conference on Machine Learning*, pp. 462–471. PMLR, 2018.

Blundell, C., Cornebise, J., Kavukcuoglu, K., and Wierstra, D. Weight uncertainty in neural networks. In *32nd International Conference on Machine Learning (ICML)*, 2015.

Cayton, L. Algorithms for manifold learning. *Univ. of California at San Diego Tech. Rep.*, 12(1-17):1, 2005.

Frazier, P. I. A tutorial on bayesian optimization. *arXiv preprint arXiv:1807.02811*, 2018.

Gal, Y. and Ghahramani, Z. Dropout as a bayesian approximation: Representing model uncertainty in deep learning. In *33rd International Conference on Machine Learning (ICML)*, pp. 1050–1059, 2016.

Ghahramani, Z. Probabilistic machine learning and artificial intelligence. *Nature*, 521(7553):452–459, 2015.

Gómez-Bombarelli, R., Wei, J. N., Duvenaud, D., Hernández-Lobato, J. M., Sánchez-Lengeling, B., Sheberla, D., Aguilera-Iparraguirre, J., Hirzel, T. D., Adams, R. P., and Aspuru-Guzik, A. Automatic chemical design using a data-driven continuous representation of molecules. *ACS central science*, 4(2):268–276, 2018.

Goodfellow, I., Pouget-Abadie, J., Mirza, M., Xu, B., Warde-Farley, D., Ozair, S., Courville, A., and Bengio, Y. Generative adversarial nets. In Ghahramani, Z., Welling, M., Cortes, C., Lawrence, N., and Weinberger, K. Q. (eds.), *Advances in Neural Information Processing Systems*, volume 27, pp. 2672–2680. Curran Associates, Inc., 2014. URL <https://proceedings.neurips.cc/paper/2014/file/5ca3e9b122f61f8f06494c97b1afccf3-Paper.pdf>.

Graves, A. Practical variational inference for neural networks. In *Advances in neural information processing systems*, pp. 2348–2356, 2011. URL <http://papers.nips.cc/paper/4329-practical-variational-inference-for-neural-networks.pdf>.

Heiss, J., Teichmann, J., and Wutte, H. How implicit regularization of neural networks affects the learned function–part i. *arXiv preprint arXiv:1911.02903*, 2019.

Hernández-Lobato, J. M. and Adams, R. Probabilistic back-propagation for scalable learning of bayesian neural networks. In *International Conference on Machine Learning*, pp. 1861–1869, 2015. URL <http://proceedings.mlr.press/v37/hernandez-lobato15.pdf>.

Kendall, A. and Gal, Y. What uncertainties do we need in bayesian deep learning for computer vision? In *Advances in neural information processing systems*, pp. 5574–5584, 2017.

Khosravi, A., Nahavandi, S., Creighton, D., and Atiya, A. F. Lower upper bound estimation method for construction of neural network-based prediction intervals. *IEEE transactions on neural networks*, 22(3):337–346, 2010.

Kuleshov, V., Fenner, N., and Ermon, S. Accurate uncertainties for deep learning using calibrated regression. In Dy, J. and Krause, A. (eds.), *Proceedings of the 35th International Conference on Machine Learning*, volume 80 of *Proceedings of Machine Learning Research*, pp. 2796–2804, Stockholm, Sweden, 10–15 Jul 2018. PMLR. URL <http://proceedings.mlr.press/v80/kuleshov18a.html>.

Lakshminarayanan, B., Pritzel, A., and Blundell, C. Simple and scalable predictive uncertainty estimation using deep ensembles. In *Advances in neural information processing systems*, pp. 6402–6413, 2017. URL <http://papers.nips.cc/paper/7219-simple-and-scalable-predictive-uncertainty-estimation-using-deep-ensembles.pdf>.

LeCun, Y., Bengio, Y., and Hinton, G. Deep learning. *Nature*, 521(7553):436–444, 2015. ISSN 1476-4687. doi: 10.1038/nature14539. URL <https://www.nature.com/articles/nature14539>.

Malinin, A. and Gales, M. Predictive uncertainty estimation via prior networks. In *Advances in Neural Information Processing Systems*, pp. 7047–7058, 2018. URL <https://papers.nips.cc/paper/2018/file/3ea2db50e62ceefceaf70a9d9a56a6f4-Paper.pdf>.

Malinin, A., Mlodzieniec, B., and Gales, M. Ensemble distribution distillation. *arXiv preprint arXiv:1905.00076*, 2019.

Malinin, A., Chervontsev, S., Prosvirkov, I., and Gales, M. Regression prior networks, 2020. URL <https://arxiv.org/pdf/2006.11590.pdf>.

Martinez-Cantin, R., De Freitas, N., Brochu, E., Castellanos, J., and Doucet, A. A bayesian exploration-exploitation approach for optimal online sensing and planning with a visually guided mobile robot. *Autonomous Robots*, 27(2): 93–103, 2009.

Neal, R. M. *Bayesian learning for neural networks*, volume 118. Springer Science & Business Media, 2012.

Nix, D. A. and Weigend, A. S. Estimating the mean and variance of the target probability distribution. In *Proceedings of 1994 ieee international conference on neural networks (ICNN'94)*, volume 1, pp. 55–60. IEEE, 1994.

Pearce, T., Zaki, M., Brintrup, A., and Neely, A. High-quality prediction intervals for deep learning: A distribution-free, ensembled approach. In *35th International Conference on Machine Learning (ICML)*, pp. 4075–4084, 2018.

Quinonero-Candela, J., Rasmussen, C. E., Sinz, F., Bousquet, O., and Schölkopf, B. Evaluating predictive uncertainty challenge. In *Machine Learning Challenges Workshop*, pp. 1–27. Springer, 2005.

Srinivas, N., Krause, A., Kakade, S. M., and Seeger, M. W. Information-theoretic regret bounds for gaussian process optimization in the bandit setting. *IEEE Transactions on Information Theory*, 58(5):3250–3265, May 2012. ISSN 1557-9654. doi: 10.1109/tit.2011.2182033. URL <http://dx.doi.org/10.1109/TIT.2011.2182033>.

Steinhilber, F., Beer, J., and Fröhlich, C. Total solar irradiance during the holocene. *Geophysical Research Letters*, 36(19), 2009. doi: 10.1029/2009GL040142. URL <https://agupubs.onlinelibrary.wiley.com/doi/abs/10.1029/2009GL040142>.

Wang, Z., Ren, T., Zhu, J., and Zhang, B. Function space particle optimization for bayesian neural networks. *arXiv preprint arXiv:1902.09754*, 2019.

Weissteiner, J. and Seuken, S. Deep learning-powered iterative combinatorial auctions. In *Proceedings of the 34th AAAI Conference of Artificial Intelligence*, pp. 2284–2293, 2020.

Wen, Y., Tran, D., and Ba, J. Batchensemble: An alternative approach to efficient ensemble and lifelong learning, 2020. URL <https://arxiv.org/pdf/2002.06715.pdf>.

Wenzel, F., Roth, K., Veeling, B. S., Świątkowski, J., Tran, L., Mandt, S., Snoek, J., Salimans, T., Jenatton, R., and Nowozin, S. How good is the bayes posterior in deep neural networks really? *arXiv preprint arXiv:2002.02405*, 2020.

Williams, C. K. and Rasmussen, C. E. *Gaussian processes for machine learning*. MIT press Cambridge, MA, 2006.